Measuring Trapped-Ion Motional Decoherence through Direct Manipulation of Motional Coherent States

by

Garrett Simon

Submitted to the Department of Physics
in partial fulfillment of the requirements for the degree of

Master of Science in Physics

at the

MASSACHUSETTS INSTITUTE OF TECHNOLOGY

June 2020

Author .....
Department of Physics
May 3, 2020

Certified by .....
Isaac L. Chuang
Professor of Physics
Professor of Electrical Engineering and Computer Science
Thesis Supervisor

Accepted by .....
Nergis Mavalvala
Associate Department Head

Measuring Trapped-Ion Motional Decoherence through Direct Manipulation of Motional Coherent States

by

Garrett Simon

Submitted to the Department of Physics
on May 3, 2020, in partial fulfillment of the
requirements for the degree of
Master of Science in Physics

Abstract

Trapped ions can serve as promising scalable qubits through the excitation of their internal electronic states with lasers to form an effective quantum two-level system, while the ion's quantized motional state in a harmonic potential well allows us to interact neighboring ions via the Coulomb force. As a result, high-fidelity operations require a precise knowledge of a system's motional decoherence time, or the time after which an ion's motional state is no longer reliably known or can no longer be controlled. Existing measurements of motional coherence indirectly control and measure the motional state by coupling the motional state to internal transitions driven by lasers, and as such, they may be prone to electronic state decoherence and laser amplitude or frequency fluctuations.

In this thesis, we apply a previously-presented mechanism of direct electric field manipulation of a trapped ion motional coherent state in a novel free precession sequence to measure motional coherence times. This sequence consists of two coherent displacements with a variable phase difference in a continuous harmonic oscillator phase-space, separated by a variable delay time. Using a strontium-88^+ ion trapped 50 micrometers above a niobium surface electrode trap in an ultra-high vacuum chamber at 4 Kelvin, we measure a motional decoherence rate of $(24 \pm 5)\ s^{-1}$. This measured rate matches the expected decoherence rate for a system where trapped ion heating dominates other forms of decoherence in magnitude, which is likely the case for our system.

Thesis Supervisor: Isaac L. Chuang
Title: Professor of Physics
Professor of Electrical Engineering and Computer Science

Acknowledgments

In science, uncertainty is something we must respect and acknowledge, as it exists in all measurements, and in quantum mechanics, as a fundamental property of nature itself. However, in this section here, I'm going to completely trash that idea, and say with 100% certainty that I would never have gotten to this point of completing an MIT advanced physics degree on my own. My initial reaction in 2018 to the complexity of research and graduate-level classes is best summarized with a quote from the beloved Forrest Gump: "I'm not a smart man." Fortunately, there were more than enough people along the way to help me through it. I could easily write an additional thesis listing all the people who have contributed to my completion of this degree, and although I'd love to do that, I'm not sure if it's the most effective use of the reader's time, so if there's anyone I failed to mention, you know who you are, and I am truly grateful for you.

This all starts with my mom and dad. Since childhood, they've taught me, through both actions and words, what it means to be disciplined and determined and how to show respect and thanks to those around you. A lot of this science stuff may not have come quickly to me, but by using these values they taught me and putting my head down, I learned that eventually it'll make sense. Thanks, you two.

The opportunity to come to MIT under the Lincoln Laboratory Military Fellows Program is a rare one, and I am grateful to all of those who took a chance and allowed me to partake in this academic adventure, before going on to do my service in the active force. To the USMA Physics department, and Dr. Lee Harrell in particular, thank you for preparing me academically for this program. To the larger USMA administration, thank you for allowing me this unique opportunity. To Mr. John Kuconis, Mr. Robert Loynd, and the Lincoln Laboratory Director's Office, thank you for heading this program for young military officers. Speaking on behalf my peers, we have learned a lot in our respective degree programs, and we look forward to sharing our experiences and expertise with the active-duty force sooner or later in our careers.

Thank you to all of the MIT physics staff and students, both graduate and undergraduate, who have helped me get through the program. Ms. Cathy Modica and Ms. Syndey Miller, you two have gone above and beyond to accommodate my unusual administrative needs as a 2-year military masters student. To the countless TA's and classmates who've had to deal with my desperate calls for help on homework assignments or test preparation, thank you. It's not an exaggeration - I absolutely would not have passed my classes without assistance and answers to my relentless barrage of questions. Professor Isaac Chuang, thank you for advising me through this process and helping me grow as both a scientist and a leader. You have helped me keep the bigger picture in mind of my development as a person, both professionally and personally. Your experience and interest in virtually all fields of science continues to amaze me, and I'm excited to see what you and the Quanta group do in the future. Professor Vladan Vuletić, thank you for serving as my academic advisor and for also being a great teacher in the classroom. I appreciate all the help and guidance you've given to keep me on track academically to graduate.

Lastly, there's the Lincoln Lab team themselves. I'm still amazed by all of your expertise, professionalism, and passion for the research you conduct. I distinctly recall being interested in your research as a senior undergrad, reaching out and inundating you with emails, then reading your publications and thinking, "these guys control single ions - they must be geniuses!" Needless to say, I was right about that. While I will never consider myself to be on the same level as you all scientifically, what was truly meaningful to me was the fact that you did everything you could to bring me up to speed and develop my confidence as a (semi-professional) physicist. John and Jeremy, you all have been there since day one, which I believe was an email from then-Cadet Garrett Simon in summer of 2017. Thank you for taking a chance on me, and letting me into this special group of really smart people. Your physics expertise speaks for itself, given your research accomplishments and how many times you've had to bail me out when I screwed something up on the experiment. More importantly though, you're great leaders who value each member of our team as individuals, and your ability to cohesively bring us together to works towards a common goal makes

all the difference. Robert, Colin, and Bob - thank you all for your continued assistance and friendliness throughout my entire stint in the ions lab. I can't count how many times I've interrupted you all in the middle of work to get help with something on the experiment or with theory, and despite the naivety of my questions, you all were more than happy to take the time to fully explain the answer. You all have helped me not just complete research, but understand research as well. Dave - where do I begin? I literally would not have been able to complete my research without your help. Realizing my tight timeline, you went out of your way to dedicate extra time towards helping me get my work done. I still consider you to be a "master of all trades, jack of none", and the everyone in the lab benefits from this. Whether it's atomic physics, mechanical engineering, electrical engineering, coding, building scientific easy-bake ovens, you've got it. Technically, I've been in the group for twice as long as you have, but I think you've contributed about 10 to 15 times the amount that I have. I am genuinely excited to see your career progress as a physicist, because I know you'll achieve whatever goals you have. Your combination of technical expertise, communication skills, and most importantly, compassion and the ability to care deeply, will take you far. Jules - I don't know how you do what you do, which is best described by the word "everything". I remember you showing me around both MIT and Lincoln Labs during my Physics open house visit in Spring 2018, and I was in awe of your sheer level of knowledge regarding AMO physics. If you hadn't told me you were a student, I would've guessed that you were full-on senior staff at the lab. Through all my trials and tribulations across the various experiment tables, you were there mentoring me during all of it. As I would learn, you're pretty much there for every experiment in the lab, which is mind-boggling considering all that we do. You have a unique ability to speak about physics in a way that's understandable to the common man (i.e. me), yet fully convey the complex science that's going on. That's something special, and I think it'll come in handy down the road in your physics career. I can't wait to see all of the research universities and labs fighting each other over who can get Jules Stuart as their quantum computing postdoc. Any lab that has you is a lab that's going to get results, and I've been lucky to have seen you in

action down in the Lincoln ions lab.

Contents

List of Figures

List of Tables

Chapter 1

Quantum Mechanics for Computation

In this chapter, we outline the origins of quantum computing by describing the fundamental physics governing this field, as well as key historical developments and applications that generated interest in quantum computing. Section 1.1 describes qubits, the basic units of a quantum computer, while section 1.2 explains the methods by which we can manipulate these qubits to perform useful algorithms. Section 1.3 describes the physical requirements for an experimental system to act as a quantum computer. Section 1.4 concludes the chapter by describing the current state of quantum computing research.

1.1 Qubits

All common modern computing devices can be labeled as "classical". They typically manipulate the voltages applied to electrical devices called transistors so that each transistor is characterized by either the presence or absence of charge, abstractly represented by the numbers 1 and 0. The state of these transistors is referred to as a bit, a hardware-agnostic term to describe any two-level system. Practical problems are then encoded binary functions that can be applied to bits. The final state of the bits then represents a solution to the practical problem, albeit still in binary representation. Although the increased density of transistors and more efficient hardware has allowed modern classical computers to solve larger and more complex problems than classical

computers of the past, a subset of computational problems remain intractable even with high amounts of computing power in the form of more bits and faster processing. Quantum computation seeks to solve these complex problems more efficiently by using fundamentally different logic operations and computation units than those of classical computers. First, instead of classical binary bits, quantum computers use quantum bits, or qubits for short. Qubits are not required to deterministically occupy the 0 or 1 states that a bit must occupy. Instead of being described solely by Boolean logic as bits are, qubits are governed by the laws of quantum mechanics. We can use these quantum mechanical properties of qubits to perform unique quantum logic operations that would be unavailable to a system using bits limited to classical Boolean operations.

The theoretical origins of quantum computing can be traced to renowned physicist Richard Feynman's 1981 keynote speech and subsequent paper on simulating physics with computers [Fey82]. Given classical computers' weakness with probability computations, Feynman argued that classical computers cannot properly simulate quantum mechanics, a probabilistic theory of nature. He instead called for a quantum computer that could serve as a "universal quantum simulator." Such a computer could efficiently simulate a quantum mechanical system since it would be built from fundamentally quantum hardware.

The theory of quantum mechanics predates Feynman's 1981 speech. This theory was created and popularized in the early 20th century, then tested experimentally through the rest of the century and still today. No test has yet disproved quantum mechanical predictions, solidifying its role as the preeminent theory describing the fundamental nature of matter. While a complete description of all quantum mechanics remains outside of the scope of this thesis, there are a few key concepts and mathematical descriptions necessary for understanding the basis of quantum computing. While quantum mechanics describes all of nature, its most counter-intuitive phenomena become evident when describing small units of matter. "Small" refers to things on the scale of fundamental particles, such as protons, electrons, and photons, quantized packets of light. Our primary quantum system of interest is an ion, which

is an atom possessing an imbalance of protons and electrons. Since many common atoms and molecules are composed of only hundreds or fewer fundamental particles, they still display the same quantum mechanical behavior of their constituent particles. However, as more and more atoms combine to form even larger, macroscopic systems, the quantum mechanical properties of their fundamental particles become less prominent. To our macroscopic eye, we instead see the behavior of the macroscopic, or "classical", system. Classical physics is best summarized by Newtonian mechanics (governed by Newton's Three Laws) and Maxwellian electromagnetism (governed by Maxwell's Equations). A transistor is one such macroscopic classical system. However, if we were to strip the transistor down and observe the behavior of the fundamental particles comprising it, we would need to discard classical physics and instead use the laws of quantum mechanics.

Given this conceptual overview of when quantum mechanics applies, one should then ask what specific quantum properties are useful for computation. The two useful properties relevant to quantum computation are (1) superposition and (2) entanglement. The first property, superposition, is one of the most prolific quantum concepts in popular science. Quantum systems, like a fundamental particle or, in our case, an ion, are described by their state, and this state can have different bases. Two common bases for a quantum object are energy or position. Superposition is the counter-intuitive ability for a quantum system to occupy multiple states at one point in time. This is forbidden in classical physics where an object can only occupy a single state in all bases, meaning that it is described with a single position, momentum, or energy. For example, a quantum object (before measurement or observation) could have two different energies or occupy more than one location. By contrast, a classical object only occupies one position and possesses one energy, regardless of whether one has actually measured the state of the object. The second property, entanglement, is the notion that multiple quantum systems, if prepared properly, can be correlated such that measurements or operations on one system can affect the other systems without any physical transfer of information between the system. This is unacceptable in classical physics; classical principles of causality and locality would require a physical

mechanism such as light, heat, or sound to transfer information between the two distinct systems. These non-classical correlations allow for multi-qubit systems to be described by joint states that enable the use logic operations which could not be performed by classical system with an equivalent number of bits.

A qubit can be physically implemented within any two-level quantum system. Those two levels are simply two distinct state values, as discussed above. Using the bra-ket notation conventionally employed in quantum mechanics, these two distinct states will hereafter be referred to as $|0\rangle$ or $|1\rangle$, analogous to the classical bit states of 0 and 1. The $|..\rangle$ notation signifies that each state is a complex-valued, two-dimensional unit vector. A complete mathematical primer on the linear algebra representation of quantum mechanics can be found at [Kri05]. Due to the property of superposition, to write the state of an arbitrary qubit denoted by the vector $|\Psi\rangle$, we cannot just write $|0\rangle$ or $|1\rangle$, which would imply that the qubit could only be measured in one possible state. Instead, we must include the complex coefficients a and b to write

$$|\Psi\rangle = a\,|0\rangle + b\,|1\rangle \tag{1.1}$$

Classically, we would only be able to have $a = 0$ with $b = 1$, or $a = 1$ with $b = 0$. In quantum mechanics, the only constraint on these complex coefficients is that

$$|a|^2 + |b|^2 = 1 \tag{1.2}$$

Another convenient, although abstract, representation of a quantum two-state system takes advantage of the fact that the coefficients a and b are complex. Since the sum of their norms squared must always equal one, they can be represented as points on the surface of a unit sphere with the basis states at the poles, referred to in physics as the Bloch sphere. Since we are now describing points on sphere, we can use the polar coordinates Θ and ϕ to equivalently describe our state vector $|\Psi\rangle$. Θ can be used to find the norm squared of the coefficients, while ϕ is used to describe the complex relative phase between the two basis states. This representation is shown graphically in figure 1-1, while the mathematical depiction of the state in equation

(1.1) is now given by:

$$|\Psi\rangle = \cos\left(\frac{\Theta}{2}\right)|0\rangle + \sin\left(\frac{\Theta}{2}\right)e^{i\phi}|1\rangle \tag{1.3}$$

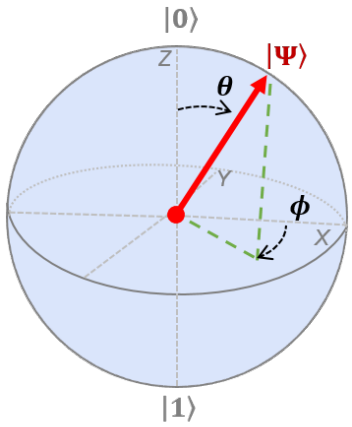

Figure 1-1: Bloch sphere representation. The state vector $|\Psi\rangle$ is shown in red on the spherical surface with radius 1. Instead of complex coordinates a and b, the state is described by polar coordinates Θ and ϕ.

One can show that the coefficients in equation (1.3) satisfy the normalization condition in equation (1.2). This notation will be particularly useful in this thesis, and in quantum computing in general. With the Bloch sphere in mind, one can easily describe changes in a qubit's state by specifying the angles by which the state has rotated around the sphere. These operations are aptly called single-qubit rotations.

While a single qubit sufficiently demonstrates our first quantum property of superposition, the property of entanglement can only be described using multi-qubit systems. A system with N-qubits requires a higher-dimensional vector space of 2^N dimensions. Some states of this larger system can be written as tensor products of its 2-dimensional subsystems, the individual qubits. States that cannot be written as a tensor product are referred to as an entangled states. As stated earlier, these states have no classical correspondence, so this linear algebra notation enables us to mathematically describe states beyond the scope of classical notation. This thesis deals

with the physics of single qubit control and does not warrant any deeper discussion on the mathematics of entangled states and multi-qubit systems.

1.2 Quantum Operations and Algorithms

Manipulating and preparing entangled superposition states, starting from our initial state definition (1.2), is achieved through the use of quantum operators, mathematically represented as $N \times N$-dimensional matrices. Properly preparing one's initial qubit states and then applying the appropriate quantum operators can manipulate the qubit state similar to classical Boolean logic operations, such as as AND, OR, NOT, CNOT, and NAND. At a minimum, a quantum computer would be capable of performing the same calculations as a classical computer by operating on qubit states that do not use superposition or entanglement. However, by appropriately preparing and entangling superposition qubit states, properly-constructed quantum operations can use qubits to perform calculations intractable on classical computers. The theoretical construction of quantum algorithms and claims of their increased efficiency over classical algorithms constitutes an entire field of mathematical physics and computer science.

While their mathematical details will not be discussed here, there are a few key algorithms whose results merit discussion. These quantum algorithms have garnered attention by requiring fewer operations than their classical counterparts to solve practical computational problems. Quantum algorithms can solve some difficult problems in "polynomial time", rather than the "exponential" time for classical computers. These times can refer to the number of operations or bits required to arrive at an answer, for a given problem size. Feynman's rule of simulation requires that the number of resources required simulate a physical system be proportional to the space-time volume of the system, preventing any physically-realizable computer, quantum or classical, from performing large-scale exponential-time computations [Fey82]. While classical computers can solve small exponential-time problems, solving larger scale problems with more bits and operations will require the use of a quantum algorithm

instead. The foremost quantum algorithm of interest is Peter Shor's eponymous algorithm introduced in 1997. His algorithm for finding prime factors of large numbers piqued the interest of national security organizations due to their reliance on the RSA encryption algorithm. RSA guarantees secure encryption by assuming that eavesdropping adversaries are unable to perform the classically difficult task of prime factorization of large numbers, thought to be an exponential-time problem. However, possessing a quantum computer would make this factorization possible in polynomial time, breaking the security of RSA [Sho97]. An equally interesting, although slightly less popularized, quantum algorithm is Grover's Algorithm. This algorithm would enable one to search an unsorted database with N-entries with a number of steps on the order of $\sqrt{N}$, while the equivalent classical algorithm would typically use on the order of N steps [Gro96]. The practicality of this speedup is obvious, assuming the database can be loaded efficiently. Although these only represent a small sample of quantum algorithms, an equally interesting premise is the possibility of discovering new algorithms and capabilities for quantum computers once the hardware exists to demonstrate these well-theorized algorithms.

It should be noted that quantum computers will likely not replace classical computers, but rather act as supplemental computational resources to solve the subset of problems where classical computers fall short. For most practical, smaller-scale problems, a quantum algorithm would require either the same or a greater number of steps than a classical algorithm. Even for minor speed-ups, the additional complexity of controlling quantum hardware and implementing quantum gates may make the classical computer faster from a practical standpoint. However, if a classical algorithm for a large-scale problem is exponential-time while a quantum algorithm for the same problem is polynomial-time, it would clearly be advantageous to possess a quantum computer. This may seem like a small and selective subset of problems, but as Shor's Algorithm and Grover's Algorithm show, solving difficult problems from this small subset can have significant practical implications.

1.3 Hardware Requirements

The purported advantages detailed above could certainly make any reader a staunch believer in the power of quantum computers. However, the physical implementation of a quantum computer is much more challenging than a classical computer. The requirements to do so are best captured by David DiVincenzo's five criteria for a physical quantum computing system [DiV00]. Since their introduction in 2000, these criteria have governed the growth of particular quantum computing platforms and accurately predicted the primary experimental challenges faced by scientists today. According to DiVicenzo, one most possess all of the following to construct and operate a quantum computer:

1. A scalable system of physical qubits, whose states can be described by a complex two-dimensional vector in the form of equation (1.1).

2. The ability to reliably initialize any qubit to a known fiducial state. This is often the $|0\rangle$ state, sometimes referred to as the ground state, but this fiducial state can vary by system.

3. Decoherence times much longer than quantum operation times, where decoherence describes any undesired interactions between a qubit and its environment or other qubits.

4. A universal set of gates that can implement any unitary transformation on a system of qubits. A unitary transformation is a special type of quantum operation, and it has been shown that one can implement these transformations by performing only single qubit rotations and two qubit XOR gates [DiV95][BBC$^+$95].

5. The ability to measure specific qubits with fidelity.

The current field of experimental quantum computing faces two overarching challenges. The first is encompassed by DiVincenzo's second through fifth criteria. The precise and reliable control and readout set forth in these criteria, even for only a few qubits, is difficult, to say the least. For experimental platforms that do manage such

immaculate control, experimenters face a second challenge of scalability, encompassed by DiVincenzo's first criterion. Properly controlling even small systems of qubits often requires a substantial experimental overhead. Only a handful of qubits may demand a room's worth of optical, electronic, or cryogenic equipment. Adding more hardware to control more qubits is technically challenging, costly, and adds more opportunities for technical errors which may decrease qubit stability and control fidelity. To perform any of the useful aforementioned algorithms, experimenters must overcome both of the two challenges by possessing equally immaculate control over even larger systems of qubits, going from currently less than 100 controlled qubits to hundreds of thousands. To enable computation despite a small, but likely inevitable, level of error, the fields of Quantum Error Correction (QEC) and Fault-Tolerant quantum computation (FTQC) seek to modify existing algorithms and preparation protocols to allow for occasional errors while still being able to compute reliable results. A comprehensive primer on QEC is given by [DMN13]. However, these improved protocols require a minimum fidelity, which is a bound on the percentage of faulty operations, and a minimum number of qubits. No existing quantum computing platform has yet achieved these thresholds [MLM+19].

1.4 Current State of Quantum Computing

Since its theoretical origins in the 20th century, a multitude of platforms have appeared as potential candidates to satisfy DiVincenzo's criteria and act as qubits for the first practical quantum computer. Some prominent systems include superconducting circuits, ions or atoms, and nitrogen-vacancy (NV) centers. Superconducting systems utilize superconducting Josephson junction circuits, where the state of the current in the circuit acts as a quantum two-level system. By applying microwaves to these circuits, experimenters can manipulate circuit states and couple the states of adjacent qubits [MLM+19]. These systems have received significant press attention over the past year, largely due to superconducting circuit research by large corporations. In early 2019, Google announced the design of a 72-qubit superconducting

processor, while later in the year, claiming "quantum supremacy" after an experimental demonstration on one of their 53-qubit processors [TQ18, AAB$^+$19]. They claimed to have sampled in approximately 200 seconds what would classically take 10,000 years to compute.

Another promising candidate for universal quantum computation are trapped ions. These systems use electromagnetic fields to confine an ion in a harmonic trap, then use the quantized motional state and the internal electronic state of the particle as qubits. Experimenters then apply microwaves or lasers to excite the internal energy state of the ion, as well as add or detract motional quanta from the ion. By coupling the internal state to the motional state of the ion, it is possible to interact neighboring ions via the Coulomb force and couple their internal spin states through their collective motion. Trapped ions have also appeared in commercial research endeavors, exemplified by the recent start-up IonQ. This company has touted their fully-connected 11-qubit quantum computer using ytterbium ions, with single-qubit and two-qubit gate fidelities of 99.5% and 97.5%, respectively [WBD$^+$19].

1.5 Outlook

This thesis research looks to contribute to experimental trapped-ion quantum computing efforts by combining existing methods of ion motion control and spectroscopy into a novel implementation of measuring motional coherence times through a free-precession sequence, which will be defined in detail in Chapter 4. We perform quantum operations by applying optical laser beams to a strontium-88$^+$ ion trapped above a surface electrode trap in an ultrahigh vacuum, cryogenic trapping chamber. In Chapter 2, we describe the physics behind ion trapping and how laser beams applied to an ion can perform quantum operations on a qubit. We also discuss how ion traps meet the hardware requirements for quantum computing as discussed earlier in Section 1.3. In Chapter 3, we delve into the experimental hardware details of our ion trapping apparatus, such as our cryocooler design, trap design, laser organization, and methods of ion state detection. In Chapter 4, we discuss the forms of decoherence

relevant to a trapped ion and show how we can mathematically represent these processes and their effects on trapped ion motional states. In this chapter, we also detail the specific free-precession sequence that we will use to measure trapped ion motional coherence. This chpater concludes with analytical models and numerical simulations to predict the results of our experimental free precession sequences. In Chapter 5, we first describe how we implement the free precession sequence in our trapped ion system. We then conclude the chapter with the measured results of our experiments and calculate a motional decoherence rate from those measurements using the models developed in the previous chapter. Finally, we conclude with Chapter 6, where we discuss the implications of our measured decoherence rate for our specific system, as well as how our measurements can apply to other systems and contribute to trapped ion quantum computing research at large. We also include a section on improvements that could be made to our experimental sequence to yield more accurate results and to compare the results of our sequence with those of other methods.

Chapter 2

Ion Trapping

Trapped ions have emerged as one of the prominent qubit platforms in research today. By choosing ions with internal energy level spacings close to the energies of microwaves and laser beams, researchers have made notable strides in turning systems of ions into addressable two-level systems for quantum computation. The origins of this method date back to Cirac and Zoller's 1995 paper [CZ95]. They presented the first physically realizable method for trapped ion computation: addressing a linear chain of cold trapped ions with laser beams and coupling them through collective motional modes. Their justification for this method also satisfied multiple of DiVincenzo's criteria [CZ95]. First, trapped ions hold some of the greatest scalability promise due to the similarity of all ions. Serving as the fundamental building blocks of matter, all atomic ions of the same species have the same energy level structure; it is impossible to have manufacturing defects in an ion. Second, current research demonstrates the feasibility of reliably initializing and measuring trapped ion qubits, satisfying the second and fifth criteria. Preparation and readout fidelities above 99.9% have been achieved by multiple experiments [HAB$^+$14, MSW$^+$08]. Third, any arbitrary quantum gate can be theoretically applied to groups of ions. It has been proven that any operation can be decomposed into 2-qubit CNOT gates and single qubit rotations, both of which have been demonstrated experimentally [SW95]. Lastly, ions display potential for negligible decoherence during computation. Ion levels with long lifetimes relative to operation times minimize the possibility of spontaneous emission during operations,

while existing research looks to improve experimental control parameters, like laser and magnetic field stability, that can affect ion coherence times [HCW+13].

In this chapter, we begin in Section 2.1 with a discussion of the Paul trap, the basic mechanism through which we trap ions using electric fields. In Section 2.2, we derive the Hamiltonian describing the interaction between the ion's internal energy levels, motional states, and an externally applied laser beam. In Section 2.3, we discuss the types of transitions used in trapped ion quantum computing to prepare the ion and perform quantum operations. In Section 2.4, we list the specific transitions and laser wavelengths required to address our specific ion, strontium-88. Finally, we conclude in Section 2.5 with the practical advantages and disadvantages of using trapped ions for quantum computation and compare our cryogenic systems with room temperature systems.

2.1 Paul Trap

Precisely trapping and controlling the motion of a single ion requires an experimental apparatus rarely seen in conventional computing. This piece of technology is the Paul trap, which earned its inventor, Wolfgang Paul, the 1989 Nobel Prize in Physics [Pau90]. This technology uses static (DC) and sinusoidally time-variant (RF) electric fields to create a confining harmonic potential well that can hold charged particles, like ions, in three dimensions. One may initially think that applying DC fields in all three directions would be sufficient to confine the ion in said directions. However, Earnshaw's Theorem, an important consequence of Maxwell's equations of electromagnetism, forbids this. Consider an ion at position (x, y, z) in a static harmonic potential characterized by

$$\Phi = \Phi_0 \left(\alpha x^2 + \beta y^2 + \gamma z^2\right) \tag{2.1}$$

Combining this potential with Laplace's Equation $\nabla^2 \Phi = 0$ requires either one or two of the three coefficients α, β, γ to be negative. Therefore, at least one dimension will be "anti-trapping," eliminating the possibility of fixing the electric field in all

three dimensions [Bro07]. Paul's solution to this problem involved fixing a static potential in one dimension while periodically varying the potential in the remaining two dimensions out of phase, creating a quasi-static three-dimensional quadrupole field (Figure 2-1(a)) [Pau90]. The orientation of this harmonic saddle potential alternates between the axes at the applied RF frequency Ω_r (Figure 2-1(b)) [Nie15].

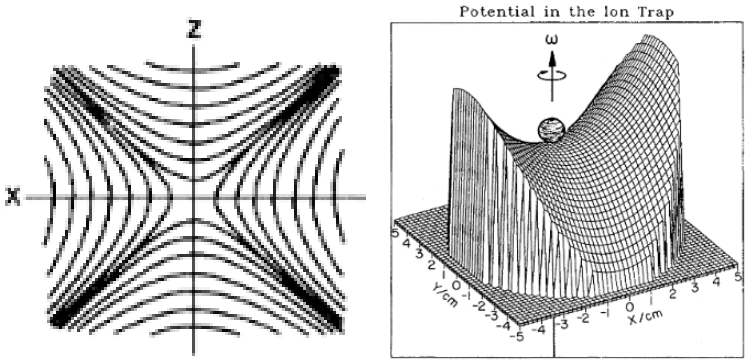

(a) (b)

Figure 2-1: Paul trap in two dimensions. (a) Equipotential lines of the quadrupole field created by the aforementioned electrodes, (b) contour plot depicting the strength and sign of the quadrupole field in two dimensions, with the ion depicted at the center. Figures taken from [Pau90].

To physically generate such a potential, a configuration of four segmented linear electrode rods can be organized as in Figure 2-2(a), with applied RF voltages $V(t) = V_0 \cos(\Omega_r t)$.

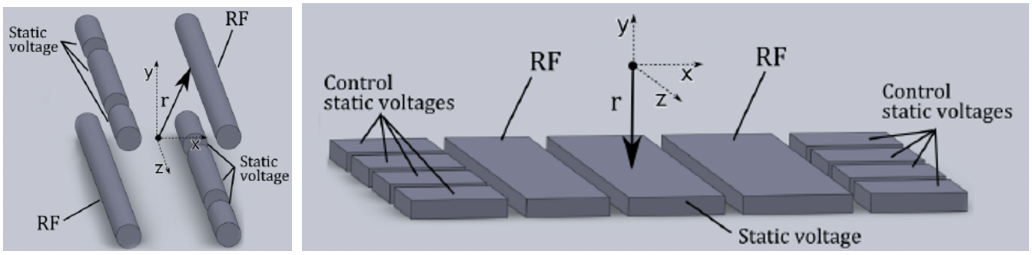

(a) (b)

Figure 2-2: Linear Paul trap electrode configurations. (a): Three-dimensional linear Paul trap created with segmented electrode rods, (b): Electrodes from the 3-D Paul trap are rearranged onto a planar surface trap. Figures taken from [SSWH11].

The ion's motion in this x-y quadrupole potential is described by a set of differential equation's outlined in Paul's original publication [Pau90]. A key result of these

equations is the appearance of a stability parameter Q, defined as $Q = 2qV_0/(mr^2\Omega_r^2)$, where q is the ion charge, m is the ion mass, and r is the distance between the center of the trap and the electrodes. Q quantifies whether the ion will remain trapped in the x and y directions; that is, it will effectively see a static quadrupole potential because it will not move quickly enough out of the anti-trapping axis before that axis changes into a trapping axis due to the fluctuating potential. For the electrode geometry shown, stable trapping is possible when we have $0 < Q < 0.908$ [Nie15]. The ion will oscillate in the x and y directions with a characteristic radial frequency $\omega_r = q\Omega_r/(2\sqrt{2})$. As a result, we can then approximate the ion's motion near the center of the trap as movement in a static, two-dimension harmonic trap, where the trap pseudopotential is given by

$$U_r = \frac{q^2V_0^2}{4mr^4\Omega_r^2}\left(x^2 + y^2\right) \tag{2.2}$$

To trap the ion in the remaining third dimension, along the z-axis parallel to the rods, one must apply static DC potentials to the electrode segments labeled "Static Voltage" in Figure 2-2(a). The configuration and number of electrode segments will determine the ion's location and movement in this "axial" direction. Similar to the radial frequency, the ion's motion along the z-axis at low energies is quantized in terms of an axial frequency ω_z which is typically less than ω_r [WMI$^+$98]. For a detailed derivation of other trap parameters like spacing for multiple trapped ions and the complete pseudo-potential derivation, see [ABLW11].

While the electrode rod configuration allows for comparatively simple control of small numbers of ions, it may face challenges when sizing up to larger-scale quantum computation. The three-dimensional rod construction would become rather cumbersome for hundreds to thousands of ions. Individually addressing the ions with laser beams also presents challenges. Some systems achieve this with individual beams focused on each ion [WBD$^+$19], but again, in the hundreds-to-thousands of qubit range, this would require many beams with precise alignment. Additionally, it would remain difficult to implement two-qubit gates between arbitrary ion pairs for such large chains

using only the Coulomb interaction, as these arbitrary gates would require controlling the collective motion of the entire chain, not only the ions of interest. However, an attractive alternative to this construction eliminates these problems with a scalable design. One can imagine flattening and laying out the 3D rods in Figure 2-2(a) to create the 2D planar surface-electrode trap design in Figure 2-2(b) [CBB$^+$05]. For appropriately sized planar electrodes, the planar surface electrode trap in Figure 2-2(b) generates the same effective potential near the RF null (where the pseudopotential is zero) as the rod configuration. This surface electrode configuration possesses numerous advantages over the prior design. First, a flat structure allows for utilization of existing microfabrication and lithography techniques used for classical electronic circuitry chips [KPM$^+$05]. Second, surface electrode trap chips allow for trapping over a variety of electrode geometries [ABLW11]. Existing research suggests that surface electrode traps could solve the aforementioned scalability issues of linear chains. One possibility includes manipulating the segmented electrode voltages to shuttle the ion into different regions to be addressed by lasers, coupled to other ions, or stored, with minimal motional excitation[BKM16, KLS$^+$20]. Surface electrode traps may also feature integrated photonics, which route laser beams using optical waveguides beneath the electrodes up through grating couplers, which focus the beams into the trapping regions [MZMH19, NSSA$^+$20]. This avoids the challenge of generating and focusing hundreds to thousands of free space beams on individual ions in a single chain.

2.2 Ion-Laser Interactions

A basic introduction into atomic physics is necessary to properly describe the dynamics of our ion-laser system, which ultimately describes how qubit states evolve in time as we apply quantum gates. A single qubit is modeled as a two-level system (the ion's 2 internal energy levels) coupled to a harmonic oscillator (the ion's motion in the Paul trap) through ion-laser interactions in the following Hamiltonian [Nie15]:

$$H = H_{internal} + H_{potential} + H_{laser} \tag{2.3}$$

For this spin-$\frac{1}{2}$ system with ground and excited basis states $|g\rangle$ and $|e\rangle$, the internal Hamiltonian is given by:

$$H_{internal} = \frac{\hbar\omega_e}{2}\sigma_z \tag{2.4}$$

where $\hbar\omega_e$ is the energy of the ion transition, expressed in terms of angular frequency ω_e, and σ_z is the conventional Pauli-z spin operator. For low motional energy states, the ion's motion is quantized as discussed above, and since we will be mostly concerned about motional excitations in the axial direction, we can define the relevant terms in the second Hamiltonian as:

$$H_{potential} \simeq \hbar\omega_z \left(n_z + \frac{1}{2}\right) \tag{2.5}$$

n_z is what will hereafter be referred to as the motional quantum number of the ion. The most complicated term in the total Hamiltonian is arguably the final component, H_{laser}. For a beam pointing along the trap axis, hence pointing in the z-direction, with wave number k and phase ϕ, the interaction is fully described by

$$H_{laser} = \frac{1}{2}\hbar\Omega_0 \left(\sigma^+ + \sigma^-\right)\left(e^{i(kz-\omega t+\phi)} + e^{-i(kz-\omega t+\phi)}\right) \tag{2.6}$$

using Pauli operators, $\sigma^\pm = \left(\sigma_x \pm i\sigma_y\right)/\sqrt{2}$, and the laser-induced Rabi frequency, Ω_0, which describes the coupling strength between the oscillating electromagnetic field and the electric dipole moment of the two ion states [Nie15, Sta04]. By transforming from this Schrödinger picture Hamiltonian to the Heisenberg picture Hamiltonian in the frame of the ion, then applying the rotating wave approximation where we neglect high-frequency terms, we have a more explanatory Hamiltonian given by:

$$H_{laser} = \frac{1}{2}\hbar\Omega_0 \left(\sigma^+ e^{i\eta\left(\tilde{a}+\tilde{a}^\dagger\right)e^{-i\Delta t}} + \sigma^- e^{-i\eta\left(\tilde{a}+\tilde{a}^\dagger\right)e^{i\Delta t}}\right) \tag{2.7}$$

where we utilize the Heisenberg creation and annhiliation operators with $\tilde{a}$ and $\tilde{a}^\dagger$, where $\tilde{a} = ae^{-i\omega_z t}$, and introduce the Lamb-Dicke parameter $\eta = kx_0 = k\sqrt{\frac{\hbar}{2m\omega_z}}$. x_0 describes the spatial extent of the ion's ground state wavefunction. The detun-

ing, $\Delta = \omega - \omega_e$, between the laser frequency ω and ion transition frequency ω_e is particularly important, as it determines the coupling between the ion's internal and motional states. Previously, the motional state, which we will denote as $|n\rangle$, and internal state, either $|g\rangle$ or $|e\rangle$, have been discussed as two distinct, non-interacting ion characteristics. However, when the detuning is approximately an integer multiple of the trap frequency ω_z, the laser will drive the transition between a specific motional and internal state. For example, given a ground state ion with motional state $|n\rangle$, written as $|g, n\rangle$, applying a laser with $\Delta \approx (m - n)\,\omega_z$, will couple the said ground state with the excited state $|e, m\rangle$ [Nie15]. This excited state has $(m - n)$ additional motional quanta than the initial state. The motional states under question affect the Rabi frequency of the transition, such that the the Rabi frequency for $|g, n\rangle \leftrightarrow |e, m\rangle$ is

$$\Omega_{n,m} = \Omega_0 \left| \langle n | \, e^{i\eta\left(\tilde{a}+\tilde{a}^\dagger\right)} \, |m\rangle \right| \tag{2.8}$$

Our particular transitions of interest are $n \leftrightarrow n$ (the "carrier" transition), $n \leftrightarrow n-1$ (the "red sideband" transition), and $n \leftrightarrow n+1$ (the "blue sideband"), with the sideband names coming from the red- or blue-shifted transition frequencies relative to the internal carrier transition frequency ω_e. These transitions are depicted graphically in Figure 2-3. In the Lamb-Dicke limit of low motional quanta, we have [Nie15]:

$$\Omega_{n,n} = \left(1 - \eta^2 n\right) \Omega_0 \tag{2.9a}$$

$$\Omega_{n,n-1} = \eta\sqrt{n}\Omega_0 \tag{2.9b}$$

$$\Omega_{n,n+1} = \eta\sqrt{n+1}\Omega_0 \tag{2.9c}$$

Solving the Hamiltonian in equation (2.7) gives second-order differential equations for the occupation probabilities of the ground state $|g, n\rangle$ and excited state $|e, m\rangle$ as a function of laser detuning and interaction time with the laser (i.e. the duration of

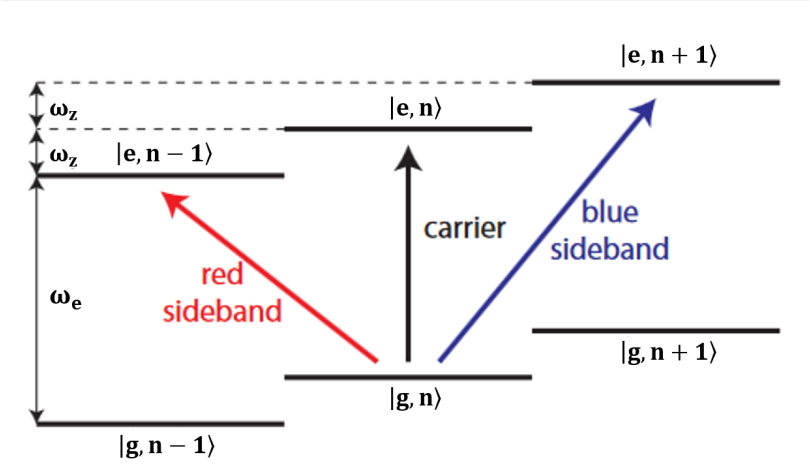

Figure 2-3: Relevant Ion Transitions. The carrier, red sideband, and blue sideband transitions for the initial state $|g, n\rangle$ are depicted between the ground and excited states. Figure adapted from [Nie15].

an applied laser pulse). The excited state occupation probability is given by [Sta04]:

$$P_{e,n\to m}(t) = \frac{\Omega_{n,m}^2}{\Omega_{n,m}^2 + \Delta^2} \sin^2\left(\frac{\sqrt{\Omega_{n,m}^2 + \Delta^2}t}{2}\right) \tag{2.10}$$

One can see that for a fixed laser strength and frequency, the excited state population will oscillate sinusoidally from 0 to $\frac{\Omega_{n,m}^2}{\Omega_{n,m}^2+\Delta^2}$ with time. Maximal excitation occurs with zero detuning and an interaction time such that $\Omega_{n,m}t = \pi$. Consequently, we denote this time t as the π-time. Analogously, applying a pulse with a duration such that $\Omega_{n,m}t = \pi/2$ puts a ground state ion into an equal superposition of the two states $|g, n\rangle$ and $|e, m\rangle$. We call this a $\pi/2$-pulse. These pulses can be conveniently represented as rotations around the Bloch sphere in Figure 2-4. While the phase ϕ of the laser is not directly reflected in the excitated population of equation (2.10), the excited and ground states will accrue a relative phase difference, as reflected in 2-4(c).

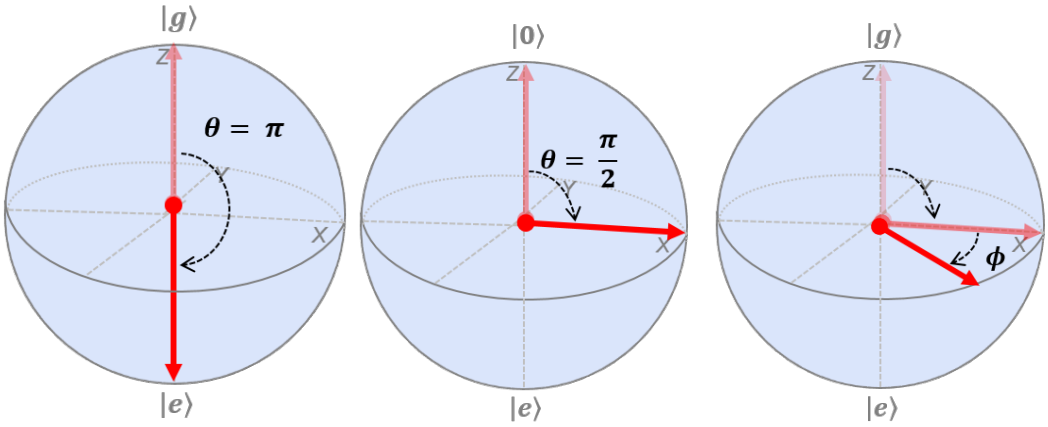

(a) π pulse (b) $\pi/2$-pulse (c) With non-zero phase.

Figure 2-4: Bloch sphere rotations for various pulse durations.

2.3 Ion State Preparation and Quantum Operations

While the development of the surface electrode trap is a remarkable feat of engineering in itself, there are multiple other state preparation techniques required for quantum operations that go beyond simply trapping the ion. In solving our ion-laser Hamiltonian, we assumed the ion was in a low motional state. Stating this more precisely, the ion must be in the Lamb-Dicke regime, characterized by the aforementioned Lamb-Dicke parameter η. For an ion with an average motional occupation number $\bar{n}$, the Lamb-Dicke regime is given by $\eta^2 (2\bar{n} + 1) \ll 1$ [Nie15]. To satisfy this inequality for our system, which has $\eta = 0.06125$, our $\bar{n}$ needs to be on the order of 1. In the absence of any Doppler cooling or sideband cooling, a single ion trapped in a surface electrode trap will possess motional quanta orders of magnitude larger than this limit, likely enough to overcome the harmonic barrier of the trap potential.

To initially cool the ion, Doppler cooling is performed. For an ion with a thermal probability distribution of energies, net cooling will occur in the presence of incoming red-detuned laser light. This means the wavelength of the light is slightly above that of the ion's internal resonant transition wavelength. As the ion moves against this radiation, it will view the incoming radiation as Doppler-shifted onto resonance, lead-

ing to absorption. Due to conservation of momentum, the ion consequently receives a momentum impulse in the direction opposite its motion. With each photon absorption, the ion will cool down until reaching its "Doppler temperature" [WI79]. At this temperature, $T_D = \frac{\hbar\Gamma}{2k_B}$, where Γ is the ion decay parameter, the Doppler cooling rate reaches equilibrium from the heating rate from spontaneous emission and other absorption processes [Sta04]. Below the Doppler limit, an alternate cooling technique

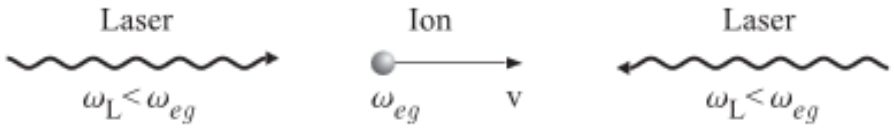

Figure 2-5: Doppler cooling in one dimension, for an ion with resonant transition frequency ω_{eg} and a laser at frequency ω_L. Figure taken from [Sta04].

known as resolved sideband cooling is employed. This technique is depicted graphically in Figure 2-6. A ground state ion $|g\rangle$ with motional occupation number n is driven to the excited state energy level $|e\rangle$, but with one less motional quanta. The excited ion will then decay back to the ground state, and the process is repeated until $n = 0$ [Pou11]. This is the aforementioned red sideband transition. By detuning the drive laser by the motional frequency, an incoming photon can only drive this sideband transition since it requires a lower energy than the carrier transition from n to n. This cooling process is possible below the Doppler temperature because sideband cooling typically utilizes a quadrupole or Raman transition with a much narrower linewidth than the Doppler cooling transition. With a narrow linewidth, one can resolve the sideband frequencies and cool on them accordingly [Pou11]. It is important to note that the ion must be in the aforementioned Lamb-Dicke regime for sideband cooling to work. A common, though by no means universal, fiducial state for most quantum operations and algorithms is the motional and internal ground state $|g, 0\rangle$. This is the fiducial state used in all experiments and operations for this work.

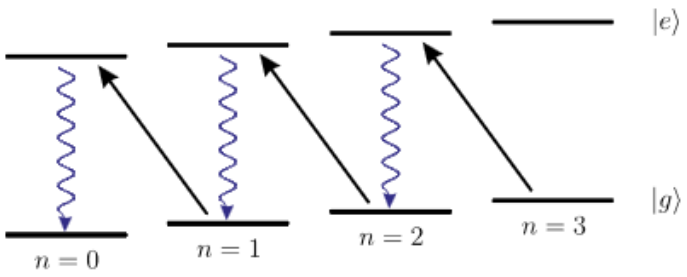

Figure 2-6: Schematic of resolved sideband cooling to the motional ground state. Figure taken from [Pou11].

2.4 The Strontium-88 Ion

The atomic level structure of the $^{88}Sr^{+}$ ion (hereafter referred to as just strontium, or Sr) determines number of lasers and preparatory operations required to ultimately drive transitions between qubit states, whether those states are motional or internal states. The initial step in preparing strontium is ionizing it. Strontium ions are not readily available on their own; they must be prepared from initially neutral strontium atoms. As depicted in Figure 2-7, a two-step photoionization process can achieve this end. An outer electron can first be excited from its ground $^1S_0$ level to the $^1P_1$ level by applying a 461-nm laser. Then, by applying a 405-nm laser, the ion is again excited to the $^1D_2$ level. This final level is auto-ionizing, meaning that the electron possesses enough energy to escape the atom without any additional applied excitation [VCLB06]. Simultaneously applying 405 and 461-nm light with overlapping beams ensures that the second transition can occur within the lifetime of the $^1P_1$ state. The broad linewidth of both transitions eliminates the need for narrow linewidth ionization laser beams [Bro07]. Strontium possesses an alkali-like level structure with 4 basic transitions required for state preparation, operations, and measurement. All of these wavelengths and linewidths can be achieved with diode lasers [Bro07]. Other transition schemes are possible, requiring alternative laser wavelengths; however, these 4 are some of the most prolific strontium operating wavelengths.

The first two relevant transitions are shown in 2-8(a). After the photoionization scheme discussed above, the outermost election is in the $2S_{1/2}$ sublevel. This electron can be driven to the $2P_{1/2}$ sublevel with a 422 nm laser. The electron will then either

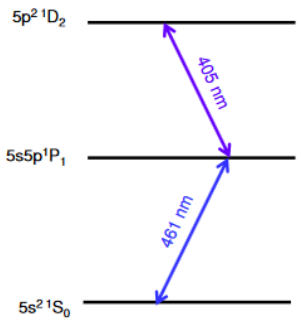

Figure 2-7: Photoionization scheme for ionizing neutral strontium atoms. Figure taken from [VCLB06].

decay back to the $2S_{1/2}$ level and emit a 422 nm photon or alternatively to the $2D_{3/2}$. In the event of this alternate decay, a "repump" 1092 nm laser is applied to drive the electron back to $2P_{1/2}$. After applying the 422 laser to an unknown ion state, a re-emitted 422 photon indicates that the ion is in the $2S_{1/2}$, while the lack of an emitted photon indicates an excited state. The broad linewidth of this 422 transition and short lifetime of 7.9 ns also makes it suitable for Doppler cooling by alternatively applying a slightly detuned 422 nm beam.

The other two relevant transitions are used to drive quantum operations and sideband cooling on the ion carrier transition, as shown in Figure 2-8(b). The carrier transition used for operations and sideband cooling is the 674 nm quadrupole transition from $2S_{1/2}$ to $2D_{5/2}$, where $2S_{1/2}$ is our ground state, often referred to as $|g\rangle$ or $|0\rangle$, and $2D_{5/2}$ is our excited state, $|e\rangle$ or $|1\rangle$. The carrier transition possesses a narrower linewidth than any of the previous transitions at 0.42 Hz, with an excited state lifetime of 390 ms [Bro07]. Although driving this quadrupole transition requires a higher laser power than the other dipole transitions, the long lifetime of the excited state ensures quantum operations can be performed in the time before the excited state decays. Single qubit operations are often on the order of microseconds (μs), while two qubit gates may last between 10-100 μs [BCMS19]. Lastly, to prevent the ion from remaining shelved in the excited state, which would otherwise require us to wait for the state to decay before performing a new measurement or initialization, a 1033 nm quench transition is used to drive the intermediary $2D_{5/2}$ to $2P_{3/2}$ transition,

after which electron will quickly decay back to the $2S_{1/2}$ ground state. From there, the ion can be cooled back to the motional ground state, leaving it initialized for a new operation and measurement [Bro07].

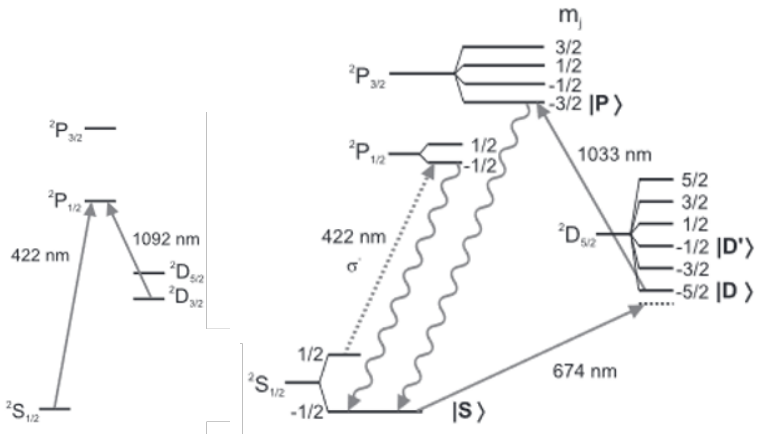

Figure 2-8: Strontium-88 ion level structure and relevant ion operation transitions. (a): Readout and Doppler cooling, (b): Quantum operations and sideband cooling. Figure taken from [Bro07].

2.5 Practical Advantages and Disadvantages

Each quantum computing platform has unique experimental requirements which determine the equipment and level of control required to achieve the requisite conditions for quantum computing. All systems have their own benefits and drawbacks, and the choice between platforms is a complex one involving scalability, cost, size, and more.

As fundamental building blocks of matter, trapped ions possess a few key properties that are ideal for qubits. As discussed earlier, the lifetime of the quadrupole transition makes it suitable for μs-timescale operations. Just as in DiVincenzo's criterion, many trapped ion systems have demonstrated coherence times longer than these operation times and others are making progress towards the times required for fault-tolerant quantum computation [BXN+17]. The uniformity of atoms is also valuable. All strontium ions of the same isotope, regardless of their number, location, or implementation apparatus, possess the same internal structure, as they are funda-

mental units of matter. While the energies of their fine and hyperfine splittings can depend on external factors like an applied magnetic field, such dependencies are well-quantified. This uniformity eliminates the challenges associated with manufacturing qubits.

The primary drawback to using a basic unit of matter is the meticulous level of control required. Isolating a single atom from any interactions with its environment is no small task. In order to utilize an atom's quantized motional state, it must be kept at low temperatures and avoid collision with ambient particles. Background collisions can excite the ion's motional mode to higher, non-thermal states which are unacceptably high for computation [CS14]. Consequently, all trapped ion systems require ultrahigh vacuum (UHV) reaching approximately 10^{-9} Torr. While these pressures can be reached at room temperature, 295 K, using cryogenics to cool the vacuum chamber to around 4 K enables the system to reach UHV much more quickly, often around 12 hours. Other advantages of cryogenic systems include reduced electrical noise and ion heating, as well as the ability to use superconducting materials. The primary drawbacks to a cryogenic trap are their additional cost and mechanical overhead, controlling of dissipated heat, vibrations from a closed-cycle cryostat, and incompatibility with standard high-temperature ion sources [ASA$^+$09].

Chapter 3

Experimental Apparatus

This chapter outlines the various mechanical and electrical components used to trap and control strontium ions. An overview of our design was originally presented in 2012 by [SKC12]. First, we describe the cryogenic UHV components of the system in Section 3.1. Next, we describe the various components within the UHV trap chamber in Section 3.2, which includes the surface electrode trap chip, which we describe in-depth in Section 3.3. We then describe our process of loading ions to the trap chip using a two-dimensional magneto-optical trap (MOT) in Section 3.4. We outline the layout of our laser beams, generated and focused external to the trap chamber, in Section 3.5. Lastly, we describe our process of imaging the ion and determining its internal state in Section 3.6.

3.1 Cryogenics and Vacuum

A hallmark of this trapping apparatus is the closed-cycle helium cryocooler, the Model SHI-4XG-15-UHV refrigerator from Janis Research Systems. This cooling system enables the trapping chamber to reach 4 K under UHV with low vibration at the sample location. Based on the Gifford-McMahon thermodynamic cooling cycle, the compression and expansion of helium gas in a closed cycle loop provides cooling near the trapping location. The system features three primary components that work in unison to achieve this task:

1. The Sumitomo Compressor. This component pumps high-pressure helium to the cold head and receives returning low-pressure helium.

2. Sumitomo RDK-415D2 Cold Head. Incoming compressed helium expands and cools in the cold head, then exits through a low-pressure line.

3. Exhange Gas Chamber. A chamber containing a helium exchange gas, which is in thermal contact with the cold head heat exchanger and the exterior of the UHV ion trap chamber.

Although the pumping of helium at a characteristic 1.2 Hz creates noticeable vibrations throughout the cold head, the use of the helium exchange gas, contained with a flexible rubber bellows, minimizes mechanical coupling to the trap chamber.

3.2 UHV Trap Chamber

The ion trap is contained in an decagonal UHV chamber with 8 indium-sealed windows allowing for optical addressing of the qubit with externally-generated free space laser beams. To go from room temperature and pressure to approximately 4 K and 10^{-9} Torr in the vicinity of the trap, multiple vacuum pumping and cooling procedures are taken. Once the chamber is closed and sealed with a copper gasket ring, high vacuum of 10^{-5} Torr is achieved through a combination of turbo-molecular pumping and an ion pump. At that point, the helium cryostat discussed above is turned on, in combination with the prior vacuum pumps, leading to crypopumping that brings the chamber to UHV. Cryopumping is the process of using cryogenic temperatures to condense any remaining gases to the coldest area of the chamber, the region in contact with the exchange gas, thereby decreasing the pressure at the more distant ion trap location. UHV is achieved within 24 hours of cryopumping, eliminating the lengthy bakeout process required for room temperature vacuum systems.

Within the chamber, the outermost layer of material encompassing the ion trap is the 50 K copper radiation shield. As indicated in the Figure 3-1, it attaches to the 50 K stage of the cold stage, keeping this shield at approximately 50 K. Its

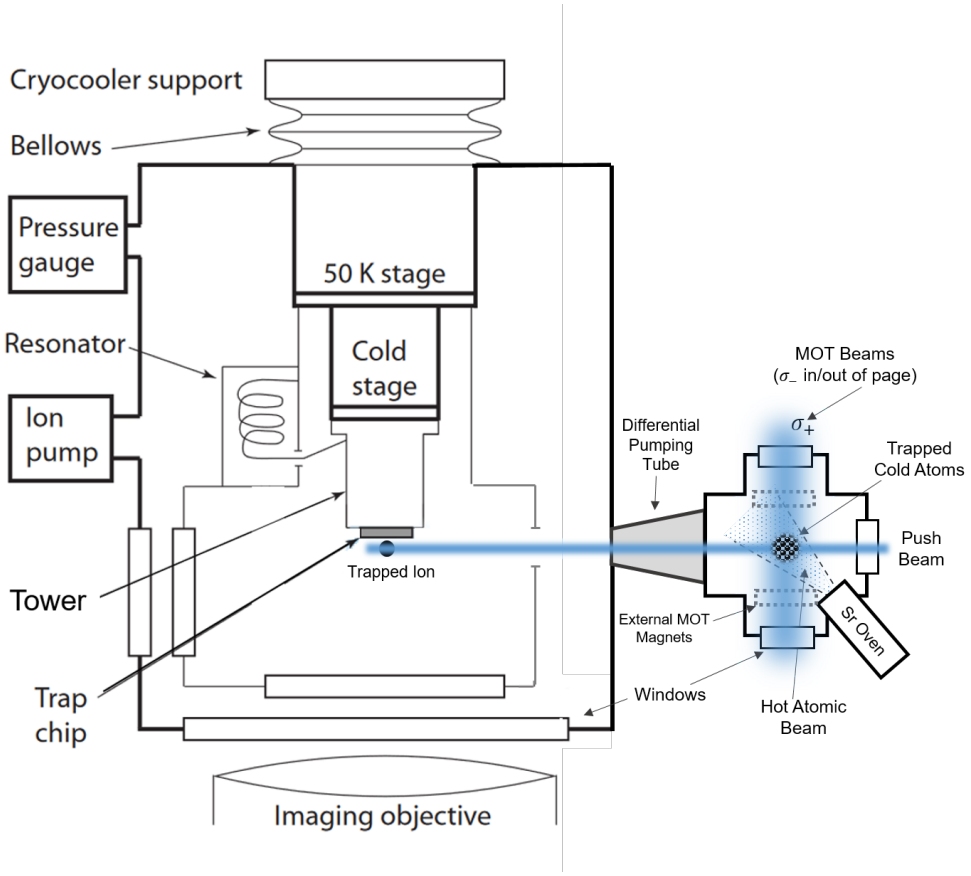

Figure 3-1: Schematic cross-section of UHV chamber containing the ion trap, adapted from the original design in [SKC12]. Not to scale. The Sumitomo compressor is not displayed, but would be located directly above the "Cryocooler support", while the Cold Head and Exchange gas chamber would be located on the inner, non-UHV interior of the regions labeled "50 K Stage" and "Cold stage". The two magneto-optical trap (MOT) beams and push beam are orthogonal.

primary purpose is to shield the trapping region from thermal radiation emitted by the chamber outer walls. It also contains a hollow cylidrical component housing a helical RF resonator used to step up the RF trap voltage sent into the chamber from the non-UHV room temperature electronics. BK7 glass windows through the shield enable optical access to the ion and imaging of ion fluorescence, while small holes located primarily near the top of the shield enable electrical feedthroughs to supply trapping voltages.

Within the radiation shield, the cold stage, a copper block, serves as the last component in thermal contact with the external exchange gas chamber, making it

the coolest region in the chamber at 4K. This block provides pathways for external electronics to pass from outside the chamber to the trap region. These electronics include DC and RF voltage wires, connections to the trap chip temperature diode, and resistive heater wires to heat the trap.

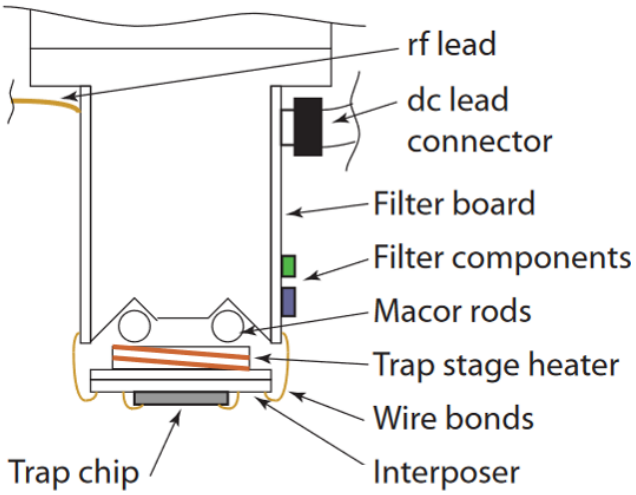

Figure 3-2: Schematic cross-section of the ion trap tower, originally presented in [SKC12]. This component can be found in the larger UHV chamber on Figure 3-1. Not to scale.

Attached to the cold stage is the final electronic and mechanical component before reaching the ion trap, the tower. A schematic cross-section is shown in Figure 3-2.. The tower serves as a mount for the chip while containing all the final electronic components and necessary connections to send voltages to the chip, heat the chip, and measure the chip temperature. It also contains a set of RC low-pass filter boards on its sides through which all DC voltages pass before going to the trap. A copper wire from the outer helical resonator passes directly to the trap. On the bottom face of the tower, there is a 1-mm thick alumina interposer with patterned gold traces. The DC voltages for each electrode are sent to a single gold trace, then these traces are connected to their respective trap electrodes via individual gold wirebonds. A microscope image of gold wirebonds connecting DC traces on the side of the tower with those on the bottom face is shown in Figure 3-3. Figure 3-4 shows the bottom of the trap, where a microscope image of the trap is surrounded by a schematic drawing

of the gold traces and temperature diode on the interposer. While the trap chip itself is attached with silver paint to the interposer, the interposer is thermally isolated from the rest of the tower through macor rod attachments. When the chamber is opened, the entire tower is disconnected from the cold stage and removed from the chamber for trap removal or attachment.

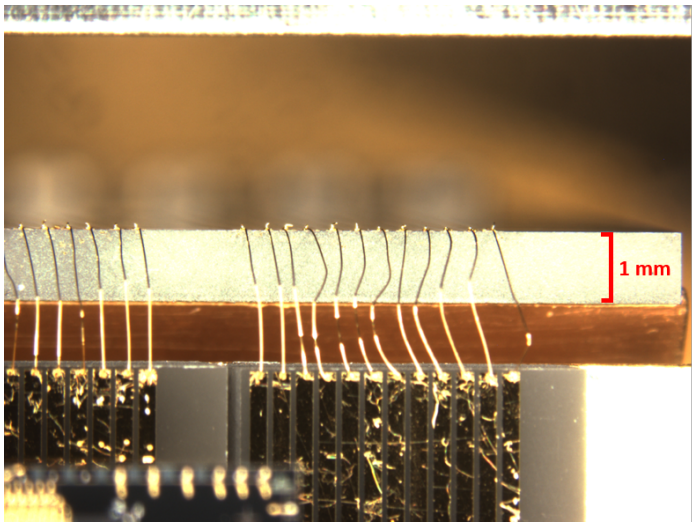

Figure 3-3: Microscope image of the tower from the side, showing gold wirebonds connecting DC voltage traces on the tower side to those on the bottom face of the tower (image is inverted; the bottom of the tower is held upwards in this image).

3.3 Surface-Electrode Trap

The surface electrode-trap is arguably the key innovation in this ion trap setup that promises scalability for replicable, large-scale quantum computers. Beyond the basic idea of having segmented electrodes etched on a conducting, two-dimensional plane, various trap designs and materials have been proposed to meet different experimental needs. Materials such as gold and niobium are often used for the outer layer of the trap, while some traps organize their electrodes to enable two-dimensional trapping and shuttling [CS14, BMCS16, KLS+20]. Our trap is composed of a 2 μm sputtered niobium layer on top of a 430 μm sapphire substrate. The electrode patterning is achieved via optical lithography at our in-house MIT Lincoln Laboratory Microelectronics Laboratory. Prior to mounting the trap on the tower, we remove excess dust

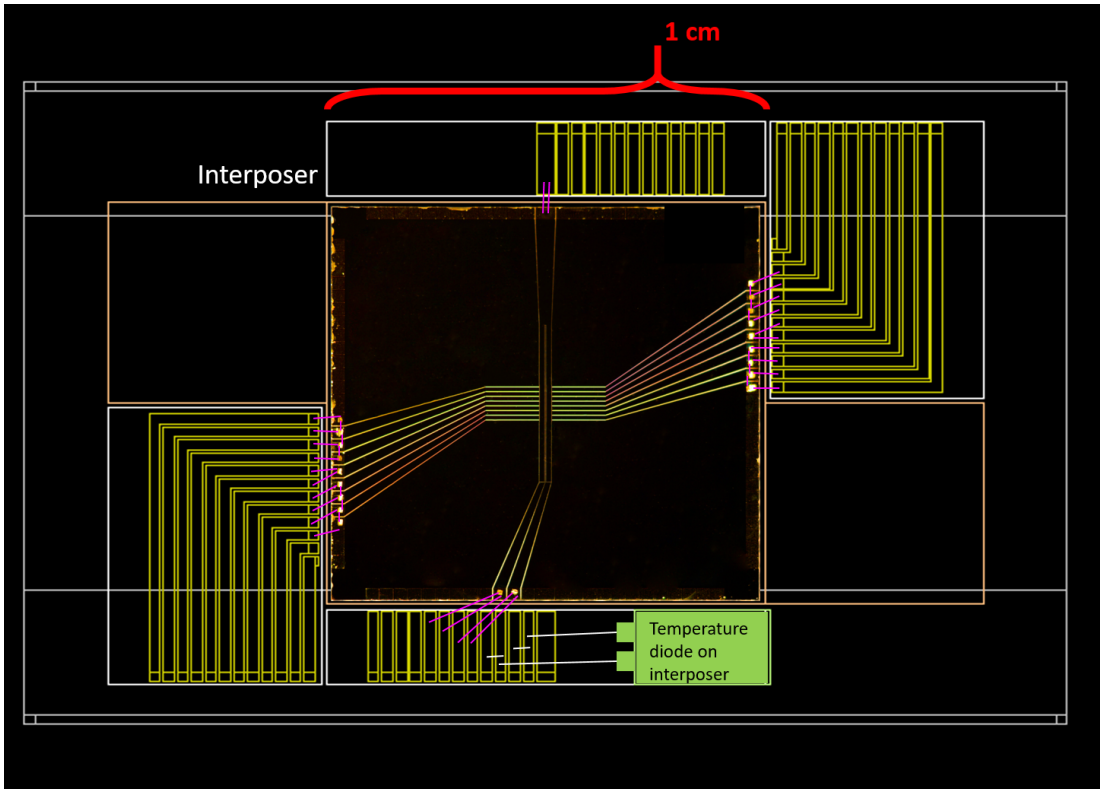

Figure 3-4: Microscope image of ion trap chip surrounded by graphical depictions of the interposer layer, with interposer electrodes (in yellow) and wirebonds from the interposer to the trap and between trap electrodes (in pink).

or particulates through a two-step acetone and isopropanol cleaning process.

As a linear trap, this trap chip displays one of the simpler electrode geometries of existing surface-electrode traps today. While a microscope image of the entire chip is shown in Figure 3-4, a detailed drawing of the electrodes at the center of the trap, near the trapping region, is shown in Figure 3-5. While there are a total of 20 DC electrodes on the trap, some electrodes are wirebonded together in a group such that they all receive the same voltage. These groups are color-coded in Figure 3-5. As a result, we only send 8 different DC voltages for these 8 electrode groups. 18 of the DC electrodes are oriented perpendicular to the trap axis, while two other electrodes, displayed in Figure 3-5 as groups 4 and 5, run parallel to the trap axis, along with the RF trapping electrodes. Given a desired axial frequency and ion position, a boundary-element simulation calculates the requisite voltages to be applied to the electrode groups, typically ranging anywhere from approximately ± 0.5 to ± 26 volts.

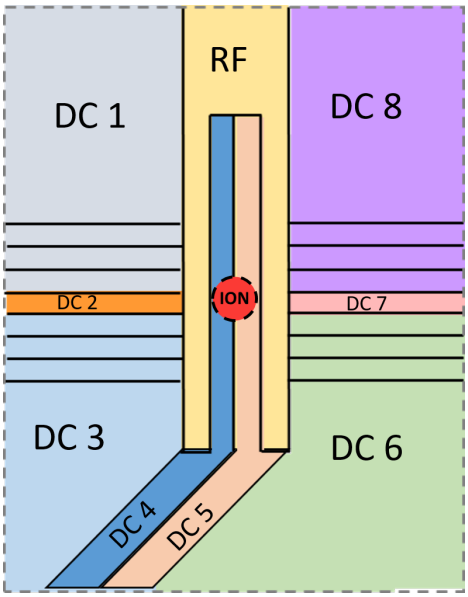

Figure 3-5: Graphical rendering of the electrode layout in the vicinity of the trapping location (center of Figure 3-4), not to scale. The RF electrode and the 8 DC groups (sets of individual electrodes all receiving the same voltage) are color-coded.

This trap holds the ion about 50 μm from its surface. To compensate for stray fields and micromotion excitations, we can add small offsets to our standard trapping voltages to shift the ion in three dimensions from sub-micrometer to hundreds of micrometer distances.

3.4 Ion Loading via 2D MOT

We use a 2-dimensional magneto-optical trap (MOT) to trap and cool gaseous strontium atoms before directing them towards the trap. This trapping technique is prolific in atomic physics, first presented in 1987 in [RPC$^+$87]. A MOT uses radiation pressure to trap and cool a cloud of neutral atoms in two dimensions. Static magnets (labeled "External MOT magnets" in Figure 3-1) are used to generate spatially-varying Zeeman splitting, in a trapping region. By heating a block of neutral strontium-88, we fill the MOT chamber with a gas of hot strontium atoms. We then send two spatially broad, circularly polarized 461 nm trapping beams in orthogonal directions such that they cross paths in the center of the trapping region, ideally where the magnetic field

is zero. These MOT beams are shown conceptually in Figure 3-1. As the hot atoms move away from the center of this trapping region, the magnetic field strength increases, and the increased Zeeman shift increases the coupling strength between their $\Delta m = \pm 1$ transitions and the MOT beams, causing them to absorb incoming MOT beam photons and receive a momentum kick back to the trap center. This traps the atoms in the two axes of the beams.

A tightly focused 461 nm push beam is sent orthogonally to the two broad MOT beams, providing a momentum kick that pushes the cold atoms along the remaining free axis through a differential pumping tube. This differential pumping tube maintains the UHV in the ion chamber despite the connection to the MOT chamber filled with hot atoms. The push beam passes 50 μm below the center of the trap chip, thereby pushing strontium atoms to the center of the trapping potential. We finally direct an overlapped 405/461 nm beam along a different axis to the same location above the ion trap through one of the UHV chamber windows. The intersection of the 461 push beam and the 405/461 beam creates a region where neutral atoms probabilistically undergo the 2-step photoionizaton process discussed earlier. If the beams are properly aligned, one of these newly created ions will be captured in the trapping potential above the chip.

3.5 Laser Organization

All laser beams are generated external to the UHV chamber, and table-mounted optics are used to focus the beams through the chamber windows into the trapping region. All beams were generated from commercial continuous-wavelength diode lasers. Acousto-optic modulators (AOMs) placed in the beam path served as the primary mechanism for switching the beams on and off and precielsely controlling laser frequencies. To achieve higher output powers on the 461 nm MOT and push beams, a 922 nm master output from a tapered amplifier is frequency doubled before being passed to a 461 nm slave diode laser. This configuration generated a total of approximately 45 mW of power, which was more than adequate for all three beams.

The 922, 1033, and 422 nm diode lasers were frequency-stabilized by locking an 852 nm laser to a cesium saturated absorption signal, then using the locked 852 laser to stabilize a Fabry Perot transfer cavity. This cavity would then serve as a reference for the aforementioned operation lasers. Due to the stability of the 405 and 1092 nm lasers, as well as the broad linewidths allowed for their respective strontium transitions, these lasers were not locked.

Due to the particular requirements of the quadrupole S-to-D carrier transition, additional components were required for the 674 laser. The carrier transition requires both a narrow linewidth and high power beam to achieve acceptable Rabi coupling frequencies and effectively sideband cool. The output of a single diode laser would be neither narrow or powerful enough to meet the 674 power distribution needs of the multiple ion trap experiments within the laboratory, leading to additional frequency locking and amplification. The 674 master output is first stabilized to an ultralow expansion (ULE) reference cavity. This cavity generates an extremely stable, narrow linewidth reference frequency used to lock our master 674 light, which injects a first slave laser, whose output injects a second slave laser. The second slave output then passes through a Toptica BoosTA tapered amplifier, delivering approximately 10 mW of power to the optical table.

Prior to reaching the trap chamber, the 422, 1033, and 674 lasers pass through a double-pass "cat's eye" AOM configuration, depicted graphically in Figure 3-6. This provides fine amplitude control and frequency control to the sub-MHz level. The advantage of a double-pass over a single-pass setup is that the double-pass output is sent in the same spatial direction regardless of the frequency by which it is shifted. The single-pass AOM output is shifted relative to the incoming by by an angle proportional to the frequency shift. The configuration includes either an Isomet or Brimrose AOM, a focusing lens, a quarter waveplate, an iris, and a mirror. Linearly-polarized input light first passes through the AOM and the lens to broaden the output, and the first-order output beam is isolated using the iris. This frequency shifted beam then passes through the quarter waveplate and reflects back off the mirror, follows the same path back to the lens, where it is focused into the AOM for a second frequency

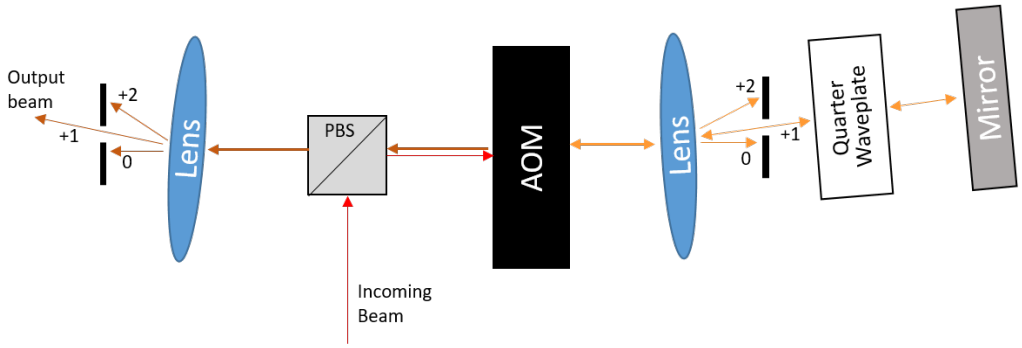

Figure 3-6: Double-pass AOM configuration. The red incoming beam first passes through the AOM, which diffracts the beam into multiple frequency-shifted orders, where zeroth, first, and second orders are shown in orange. The first order is isolated with an iris and sent along the same path back through the AOM, where it is again frequency shifted into multiple orders shown in brown. The PBS separates the outgoing from the incoming beam, and another iris isolates the frequency shifted first-order beam.

shift. The first-order frequency-shifted beam after this second pass will always exit the AOM at the same angle, regardless of the total frequency shift. The first order is isolated with an iris external to the double-pass configuration, and the output beam is isolated from the counterpropagating input beam with a polarizing beamsplitter, as it has shifted its polarization 90 degrees due to the two quarter waveplate passes.

3.6 Imaging and State Detection

As discussed previously in Section 2.4, the 422 nm S-to-P transition is used for state-dependent fluorescence, in combination with the 1092 nm repumping transition. Circular windows are placed on the bottom faces of the 50 K radiation shield and the UHV chamber to allow emitted 422 photons from the $2P_{1/2}$ state to escape the chamber. From there, an external imaging objective lens close the UHV lower window collects a large solid angle of the emitted light and focuses the image of the trap and the ion to a motorized flipper mirror mount. This mirror can direct the light into either a Princeton Instruments ProEM 512 CCD camera or a Picoquant PMA Series photomultiplier detector assembly. A 422 nm optical filter is used to eliminate background light at the detection devices, while an iris is closed around the focused image

to block scattered light from the 422 nm beam. Figure 3-7 displays the CCD image of the ion. To determine the ion state as bright ($2S_{1/2}$ or $|g\rangle$) or dark ($2D_{5/2}$ or $|e\rangle$), we

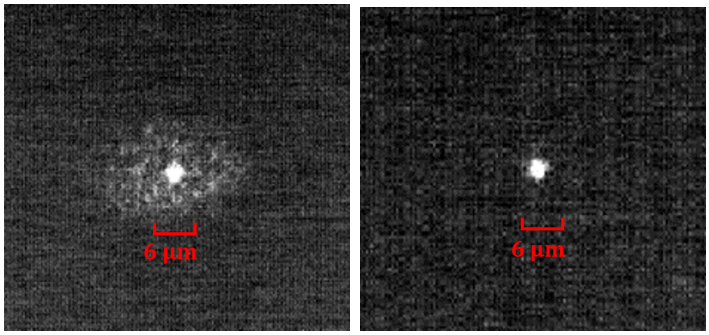

(a) With 422 scatter (b) Without scatter

Figure 3-7: Images of ion from CCD camera. 3-7(a) shows the iris closed around the ion with addition 422 beam light intentionally being scattered from the trap surface for comparison. 3-7(b) shows the same iris closure, but without intentional 422 scatter.

take a series of shots where we apply a 422 nm laser pulse and record the number of photon counts from the PMT. For each shot, the number of detected photons follows a normal distribution, so plotting the number of counts for all shots on a histogram will manifest as either one or two distinct Gaussian distributions. If the ion is in the dark state, no photons are emitted, and the count distribution on the histogram will reflect the background detections by the PMT. If the ion is in the bright state, the histogram count distribution will be centered about a higher number of counts than that of the background count distribution. If the ion is in a superposition of bright and dark, two histograms will appear, centered at both the bright state mean counts and the background mean counts. The fraction of detections falling into either the upper or lower histogram distribution determines the occupation probabilities. This technique relies on our ability to resolve the background and bright state histograms.

Chapter 4

Motional State Free Precession Sequences

In this chapter, we outline our novel application of trapped ion motional coherent state manipulation, originally presented in in [MKW+19], for implementing free precession sequences to measure decoherence rates. Prior methods of motional state manipulation commonly involved using internal state sideband transitions to indirectly manipulate the ion's motional state [dMFV96, Zhe98]. Others used a technique of modulating the applied Doppler cooling laser to manipulate the ion's motional state to generate displaced thermal states [TGD+16]. Our method, hereafter referred to as coherent driving or electric field displacement, applies an additional RF voltage to the trap electrodes, creating a resonant electric field perturbation that directly applies a motional force to the ion, displacing it in phase space. In this manner, the only coupling between the motional and internal states of the ion occur during initialization to the ground state and during state readout, which utilize either Doppler cooling and a series of red sideband pulses or a single pulse. All motional state manipulation is done through the electric drive field.

However, to establish the context and theory necessary to describe the free precession sequences we perform with the aforementioned motional state manipulation, we first describe the existing models for motional states and decoherence processes, which we will later use to simulate the results of our free precession sequences. In

Section 4.1, we describe harmonic oscillator coherent states and explain how they are generated through our electric field displacements. In Section 4.2, we describe the concepts and formalisms of open system dynamics, which we can use to describe various types of decoherence processes relevant to our trapped ion system. Then, in Section 4.3, we delve into the specifics of our free precession sequences, describing their origin in two-level spectroscopy sequences, explaining how to implement them experimentally, presenting advantages of our method, and finally, deriving the model equations to predict the results of free precession sequences for various decoherences processes. We conclude the chapter with Section 4.4, where we explain the method by which we read out the motional state of the ion by mapping the motional state onto the internal excited state probability, which we can then detect using our conventional state-dependent fluorescence methods.

4.1 Coherent States and Motional Coherence

The coherent state is a useful mathematical tool for describing quantum harmonic oscillators, such as the ion's quantized axial motion. While their notation and use fully obeys the laws and conventions of quantum mechanics, coherent states reflect the most "classically-possible" quantum state by replicating classical behavior through their expectation values and possessing minimal uncertainty. In one dimension, the coherent state position and momentum expectation values $\langle q \rangle$ and $\langle p \rangle$ obey the classical harmonic oscillator equations of motion, while also saturating the Heisenberg Uncertainty limit of $\Delta q \Delta p = \hbar/2$ in any one dimension q [HR87].

Coherent states are parameterized by a complex value α, allowing us to denote them as $|\alpha\rangle$. They are also eigenstates of the harmonic oscillator destruction operator $\hat{a}$ such that

$$\hat{a} |\alpha\rangle = \alpha |\alpha\rangle \tag{4.1}$$

The quantum harmonic oscillator Hamiltonian is given by $H = \hbar\omega\hat{a}^\dagger\hat{a}$, and the expectation value of the number operator $\hat{N} = \hat{a}^\dagger\hat{a}$ gives the average occupation number $\bar{n}$ of the coherent state $|\alpha\rangle$. We find $\langle N \rangle = \langle\alpha| \alpha^*\alpha |\alpha\rangle = |\alpha|^2$, so the average occupation

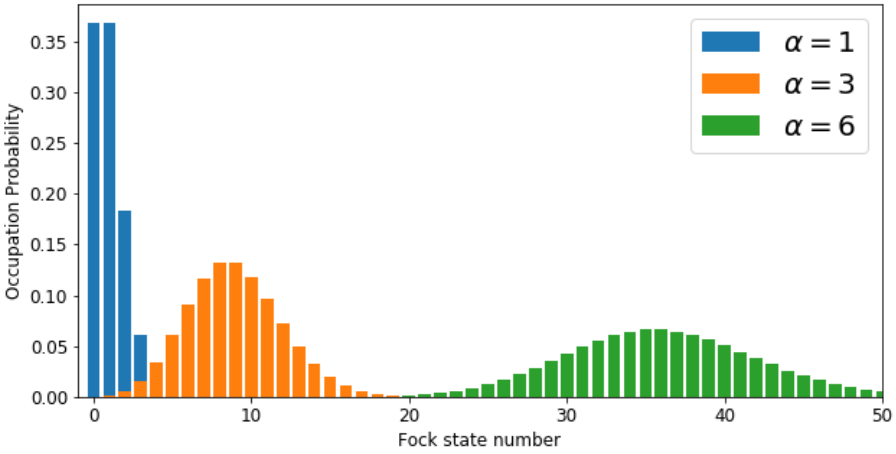

Figure 4-1: Occupation probabilities in the Fock states $|n\rangle$ basis given coherent state characterized by α. The probabilities are distributed in accordance with Eq. (4.4).

number for a coherent state $|\alpha\rangle$ is $\bar{n} = |\alpha|^2$.

The coherent state is generated the unitary displacement operator

$$\hat{D}(\alpha) = \exp\left(\alpha\hat{a}^\dagger - \alpha^*\hat{a}\right) \tag{4.2}$$

Applying the displacement operator with a given complex value of α to $|0\rangle$ returns the coherent state $|\alpha\rangle$, written in the Fock basis as [CN65]

$$|\alpha\rangle = \sum_{n=0}^{\infty} \frac{e^{-\frac{1}{2}|\alpha|^2}\alpha^n}{\sqrt{n!}} |n\rangle \tag{4.3}$$

This notation displays that $|\alpha\rangle$ is actually a superposition of all harmonic oscillator number states, or Fock states, indexed here by $|n\rangle$. The normalized probabilities of measuring the coherent state in any one of these levels are Poisson distributed, meaning that they obey the following probability distribution, which is displayed in Figure 4-1:

$$P_n(\alpha) = \frac{e^{-|\alpha|^2}|\alpha|^{2n}}{n!} \tag{4.4}$$

These coherent displacements can be physically implemented by coupling a harmonic oscillator at frequency ω_z to a sinusoidal driving force at frequency ω. The

resultant value of α will depending on the coupling time, strength, and frequency of this driving force. The harmonic oscillator Hamiltonian can be appropriately modified to reflect this interaction by including a time-dependent term. For our purposes, the driving force comes from an electric field $E(t) = E_0 \cos(\omega t + \phi)$ acting on a charged particle. As such, the driven system Hamiltonian is given by

$$H = \hbar\omega_z \hat{a}^\dagger \hat{a} + qE_0 \cos(\omega t + \phi) z_0 \left(\hat{a}^\dagger + \hat{a}\right) \tag{4.5}$$

where we have utilized the ground state harmonic oscillator extent $z_0 = \sqrt{\hbar/(2m\omega_z)}$. We will now quantify the drive field coupling strength with the Rabi frequency $\Omega_0 = qE_0 z_0/(2\hbar)$. Assuming the detuning between the two frequencies $\delta = \omega - \omega_z$ is sufficiently small, we can switch to the rotating frame of the oscillator and neglect high frequency terms, giving us a simpler Hamiltonian in the interaction frame [MKW+19]:

$$H = \hbar\Omega \left(\hat{a}^\dagger e^{-i(\delta t+\phi)} + \hat{a} e^{i(\delta t+\phi)}\right) \tag{4.6}$$

In the absence of any decoherence or dephasing processes, coherent states and displacements can be described by unitary evolution of state vectors [SW10]. Using the Schrödinger equation, subjecting an initial coherent state $|\alpha(t_0)\rangle$ to the interaction Hamiltonian above for duration t gives the final state $|\Psi(t)\rangle = |\alpha(t)\rangle$. This is a displaced coherent state described using the displacement operator as

$$|\alpha(t)\rangle = \hat{D}(\alpha(t)) |\alpha(t_0)\rangle \tag{4.7}$$

In the case of a time dependent detuning $\delta(t)$, a solution $\alpha(t)$ can be conveniently derived, as in [MKW+19]:

$$\dot{\alpha}(t) = \alpha(t) i\delta(t) + \Omega e^{i\phi} \tag{4.8}$$

$$\alpha(t_0, \tau) = e^{i\int_{t_0}^{t_0+\tau} \delta(\tau_1) d\tau_1} \left[\alpha(t_0) + \Omega e^{i\phi} \int_{t_0}^{t_0+\tau} e^{-i\int_{t_0}^{\tau_2} \delta(\tau_1) d\tau_1} d\tau_2\right] \tag{4.9}$$

By modifying the parameters and recursively using equation (4.9), we are able to determine the final coherent state after a sequence of electric field drives and free

evolution periods.

4.2 Open-System Dynamics

In the likely event of decoherence or environmental interactions, one will need to describe the evolution of a coherent state as open system dynamics, requiring the use of density matrices to represent the oscillator state. Unitary evolution of state vectors through the Schrödinger equation only allows population to transfer between the levels of the state vector, not to any other systems or states. Unwanted interactions with the environment that result in loss of population or phase coherence are reflected in the off-diagonal coherences of density matrices. The density matrix ρ for a state vector $|\Psi\rangle$ is given by

$$\rho = |\Psi\rangle \langle\Psi| \tag{4.10}$$

Applying the Schrödinger equation to a density matrix gives the master equation for its time evolution as the following [SW10]:

$$\frac{\partial \rho}{\partial t} = \frac{1}{i\hbar} [H, \rho] \tag{4.11}$$

However, this alone is not adequate to enable non-unitary evolution of the density matrix. Equation (4.11) only considers the internal dynamics of the system. To consider interactions with the environment, we must include correction terms $\hat{L}_k$, known as Linblad operators, where k is an index over all operators being considered. These operators must be constructed specifically to represent an open system interaction of interest. By including them in Equation (4.11), we arrive at the master equation in Linblad form:

$$\frac{\partial \rho}{\partial t} = \frac{1}{i\hbar} [H, \rho] + \frac{1}{2} \sum_k \left(2\hat{L}_k \rho L_k^\dagger - \hat{L}_k^\dagger \hat{L}_k \rho - \rho \hat{L}_k^\dagger \hat{L}_k \right) \tag{4.12}$$

4.2.1 Decoherence Processes

As a quantum state couples to its environment, unwanted interactions degrade the fidelity of the isolated quantum state by altering the relative magnitudes or phases between levels, and the system typically tends toward a thermal equilibrium with the environment. This process is generally referred to as decoherence. Coherent states, or superpositions of these oscillator number states, are sensitive to these processes, and if unwanted interactions allow them to reach environmental thermal equilibrium, the original Poisson number state distribution and off-diagonal density matrix coherences will be replaced by a thermal distribution of states determined by the temperature of the environment.

Relevant decoherence processes to our quantum harmonic oscillator can be categorized as amplitude damping and phase damping processes. Amplitude damping, sometimes called relaxation, involves the transfer of energy between the system and a larger thermal reservoir. For the harmonic oscillator, this transfer of energy manifests as the creation or annihilation of motional quanta. This alters the number state distribution of a given harmonic oscillator state. The mathematical form of such processes will be discussed in the following subsection. Phase damping processes, on the other hand, do not change the energy of the system. They only affect the relative phases between the oscillator levels, leading to a exponential time decay of the off-diagonal density matrix elements [TMK$^+$00]. Such processes include fluctuations in the harmonic oscillator frequency. Following the convention in [TMK$^+$00], Linblad operators for dephasing processes are generally described by $\hat{L} = \sqrt{\kappa}\hat{a}^\dagger\hat{a}$, where κ is the dephasing rate.

In a two-level system, relaxation and dephasing are quantified time constants T_1 and T_2, respectively, which describe the exponential decay of an excited state and off-diagonal matrix elements with time as the systems tends to thermal equilibrium. A two-level system's decoherence times are bounded by the inequality $T_2 \leq 2T_1$. Since T_1 relation processes contribute to dephasing, T_2 is defined as $1/T_2 = 1/(2T_1)+\Gamma_\phi$, where Γ_ϕ represents the rate of "pure dephasing" processes. One can see that additional

pure dephasing decreases T_2 from its maximal value of $2T_1$ [JC12].

4.2.2 Trapped Ion Heating

One particular decoherence process of interest in our system is trapped ion motional heating, a form of amplitude damping where electric field fluctuations exert uncontrolled Coulomb forces, effectively "heating" the ion by exciting it to higher motional states in its harmonic potential. This is one of the major sources of decoherence in trapped ion systems [IMPM03]. Measured in quanta per second (q/s), measured heating rates are often orders of magnitude larger than what would be caused by common sources of electric field fluctations, like Johnson noise from electron motion in the electrode metals [BKW18]. The quanta/s units, hereafter given as q/s, refer to the number of motional quanta the harmonic oscillator gains or loses per unit time. Motional heating can degrade the fidelity of multi-qubit gates, which rely on precise motional control for ion coupling [Bro07]. While a widely-applicable explanation for the physical mechanism of trapped-ion heating remains unknown, its effects on quantum harmonic oscillator coherence can be generalized as a amplitude damping process.

One such amplitude damping description uses the master equation below, Equation (4.13), originally presented in [IMPM03]. This equation treats the heating process as a single trapped ion harmonic oscillator coupled to a thermal reservoir, modeled as an infinite chain of quantum harmonic oscillators at thermal equilibrium at temperature T.

$$\frac{\partial \rho}{\partial t} = -\Gamma\left(N+1\right)\left(\hat{a}^\dagger\hat{a}\rho + \rho\hat{a}^\dagger\hat{a} - 2\hat{a}\rho\hat{a}^\dagger\right) - \Gamma N\left(\hat{a}\hat{a}^\dagger\rho + \rho\hat{a}\hat{a}^\dagger - 2\hat{a}^\dagger\rho\hat{a}\right) \tag{4.13}$$

Γ is the heating constant, in units of inverse time, while N is the average number of thermal excitations in the reservoir, which is a function of T. One can see that this equation is equivalent to the Linblad form of (4.12) using Linblad operators $\hat{L}_e = \sqrt{2\Gamma\left(N+1\right)}\hat{a}$ and $\hat{L}_a = \sqrt{2\Gamma N}\hat{a}^\dagger$ and going to the reference frame of the oscillator to eliminate the Hamiltonian commutator term in Equation (4.12). $\hat{L}_e$ represents

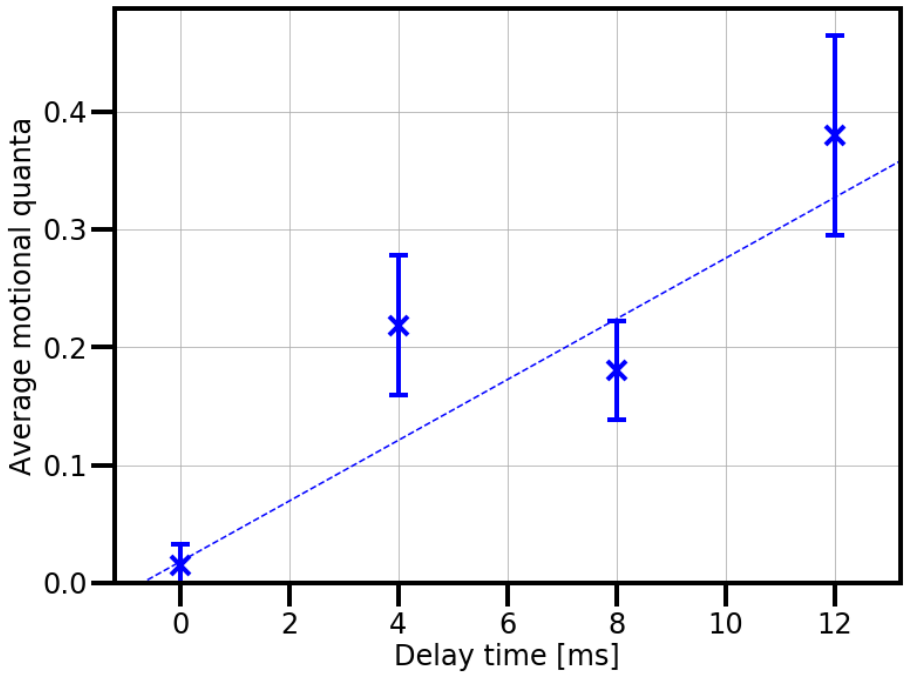

Figure 4-2: Fitted experimental heating rate of (26 ± 5) q/s, determined using sideband ratio spectroscopy.

emission processes where the ion loses motional quanta, while $\hat{L}_a$ corresponds to absorption processes where the ion gains motional quanta from the reservoir [IMPM03]. By using a measured trapped ion heating rate for Γ, we can model the time evolution of a system subject to motional heating modeled as amplitude damping.

One method for measured heating rates uses sideband ratio spectroscopy. As discussed earlier in this thesis, our use of the narrow quadrupole transition from $2S_{1/2}$ to $2D_{5/2}$ enables us to resolve the ion's first-order motional sideband frequencies. Due to the thermally distributed motional state occupation probabilities, in the Lamb-Dicke limit, the ratio R of the RSB and BSB frequency line amplitudes is related to the mean occupation number of the ion's thermal state according to $\bar{n} = R/(1-R)$ [ESL+07]. Measuring this sideband ratio after allowing the ion to freely evolve over a range of delay times gives the heating rate. One measured heating rate for our system was (26 ± 5) q/s, and the motional occupation numbers after various delay times are shown in Figure 4-2.

4.3 Free Precession Spectroscopy Sequences

One common method for quantifying trapped ion decoherence involves allowing the ion to freely evolve during a fixed precession time, then interfering the final state with the initial state before the precession time. Originally developed in the mid-20th century by Norman Ramsey, the method is central to high-resolution measurements of transition frequencies in atomic clocks. Later modifications have made it an invaluable tool for measuring relevant coherence parameters for quantum information studies, particularly for 2-level transitions. The measurement involves applying an interaction field for time τ on some 2-level transition spaced by a characteristic frequency, waiting a free precession period, also referred to as a delay period, T, then applying another interaction pulse of time τ [ATdS$^+$16]. By varying the frequency of the interaction pulses, the delay time, or the phase difference between the pulses, different properties about the system and the transition frequency can be obtained.

Our research, however, focuses on higher-dimensional motional states, so we will need to modify this two-level Ramsey free precession sequence to gain information about our system. In this section, we derive a mathematical model for our motional state free precession sequences, which are analogous to the prolific 2-level Ramsey spectroscopy sequences discussed above. In subsection 4.3.1, we first describe more details on how Ramsey spectroscopy can probe decoherence processes in a two-level system to develop intuition for free precession spectroscopy. In subsection 4.3.2, we move to the specifics of our research by describing the steps of the coherent state free precession sequence itself. We first describe how the sequence can be implemented experimentally. We then develop the sequence mathematically by phenomenologically modeling the expected results for the cases of no decoherence, amplitude damping, and dephasing, and finally with a more rigorous numerical simulation of a motional state during the sequence using open-system dynamics.

4.3.1 Internal State Ramsey Spectroscopy

Trapped ion experiments have implemented the Ramsey method for a variety of two-level systems. Examples include the ion internal states $|g\rangle$ and $|e\rangle$, motional Fock states $|n\rangle$ and $|n+\Delta\rangle$, and even cat states, which are superpositions of motional coherent states [RCM+08, LGRS04, TMK+00]. A brief discussion of the internal state Ramsey sequence is warranted, since it is particularly common and quite intuitive. The two states $|g\rangle$ and $|e\rangle$ are separated by the transition frequency ω_0. A $\pi/2$ pulse at the carrier frequency on the initial state $|g\rangle$ puts the system in $|g\rangle + |e\rangle$ (omitting normalization). In the reference frame of the ion, rotating at ω_e, fluctuations in either the trap or laser frequency during the delay time T will manifest as a phase $\phi(T)$, whose time dependence is governed by the form of the frequency fluctuations. The state is now $|g\rangle + e^{i\phi(T)}|e\rangle$ before the application of another $\pi/2$ pulse, which has the phase Φ relative to the first pulse. This is represented graphically on the Bloch sphere in Figure 4-3.

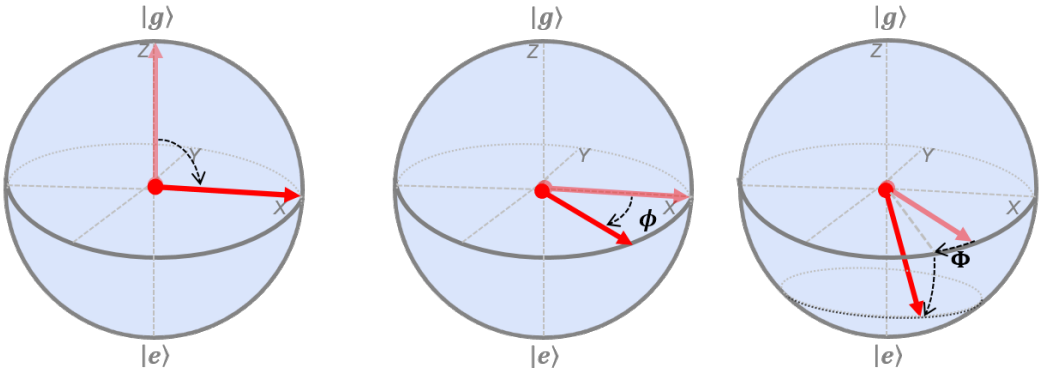

Figure 4-3: Internal State Ramsey Sequence. From left to right, the three sequences of a Ramsey sequence on the ion internal state transition are displayed: the initial $\pi/2$ pulse, relative phase accumulation ϕ during delay time T, and a second $\pi/2$ pulse with an applied phase Φ.

Information about the system can be gained through three variations of the Ramsey sequence. These include varying the $\pi/2$ pulse frequency ω, the delay time T, or the pulse phase difference Φ. Each experiment will display a characteristic line-

shape. The research in this thesis primarily deals with the variation of both the phase difference and delay time while keeping the pulse frequency on resonance, as most trapped ion experiments do. The excitation probability as a function of Φ will oscillate sinusoidally with a 2π period, and the contrast of these oscillations (peak minus trough amplitude) will depend on the Ramsey delay time T and the noise features of the system, as exemplified in Figure 4-4. Plotting the oscillation contrast versus the Ramsey delay time shows that the contrast follows an exponential decay $\exp(-T/T_2)$ parameterized by a time constant T_2 [LKH$^+$07]. As the ion freely precesses for times near and beyond T_2, decoherence processes that affect the phase relationship between the two levels, frequency fluctuations in particular, will become evident [Chw09].

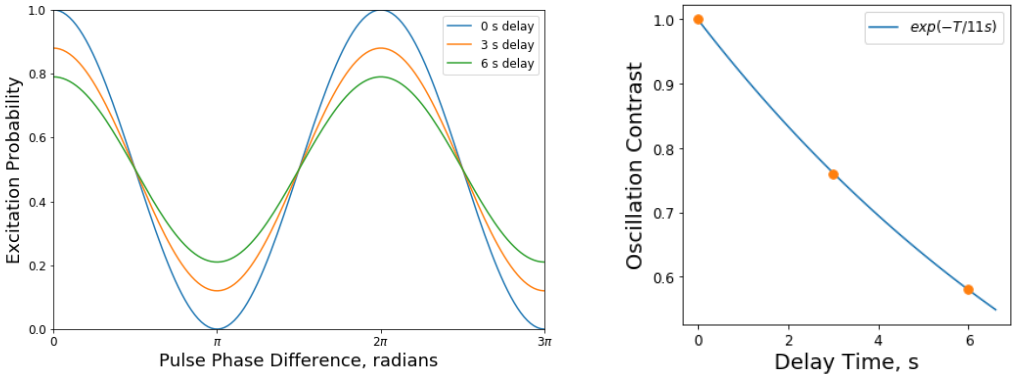

(a) Ramsey Oscillations (b) Ramsey Contrast Decay

Figure 4-4: Properties of a Ramsey sequence for an arbitrary theoretical 2-level system with $T_2 = 11\ s$. (a) Ramsey oscillations are plotted for various delay times; (b) the corresponding contrast decay for the oscillations shown in the adjacent graph. These simulated graphs do not represent any actual data or system under consideration.

Although the research in this thesis will use a different quantum system for Ramsey spectroscopy, namely the quantum harmonic oscillator in the form of motional coherent states, the theory and measured results remain fundamentally similar to those of a two-level system. The concept of measuring a decoherence time through the exponential decay of Ramsey oscillation contrast is the key takeaway from this discussion. The lineshapes and equations displayed in Figure 4-4 will appear multiple times throughout the rest of this thesis.

4.3.2 Coherent State Free Precession Sequences

While the context of the two-level free precession sequence is useful, we now need to apply that background to the motional states. We propose a novel mechanism of motional coherence measurement via free precession sequences on coherent states manipulated using the aforementioned electric drive field method. Our free precession sequences differ from the analogous 2-level Ramsey sequence since they does not create any interference between two distinct quantum states, which would imply an effectively two-dimensional Hilbert space. Instead, we measure the coherence of a single motional state relative to a stable reference oscillator (the drive field) as it freely evolves. By performing coherent drives, characterized by α, in place of the conventional $\pi/2$ pulses in a spin-1/2 Ramsey sequence, we act only on a single motional coherent state. Over the duration of the drive, the state moves classically though a position-momentum phase space then occupies a different final state. The displacement of a harmonic oscillator coherent state in a continuous phase space is arguably the most classical description possible of a quantum system, yet we can still observe quantum interference results identical to those of a conventional two-state superposition. Analogous to the Bloch sphere representation for a two-level system in Figure 4-3, the three parts of our free precession sequence are displayed graphically in Figure 4-5.

This method of motional state manipulation via coherent displacement (presented in [MKW$^+$19]) has been studied in other works, but to the best of our knowledge never been explicitly used for a free precession sequence capable of quantifying motional decoherence [LMM$^+$98, WSH$^+$19]. Similar free precession sequences have been performed through modulation of the Doppler cooling laser to displace thermal motional states [TGD$^+$16], but without this capability to directly modulate the harmonic potential as in our implementation. To our knowledge, we are the first to perform these sequences and observe Ramsey-like oscillations by varying the relative phase between the two coherent displacements. The thermal state sequences in [TGD$^+$16] observed such oscillations by increasing the delay time between in-phase displacements.

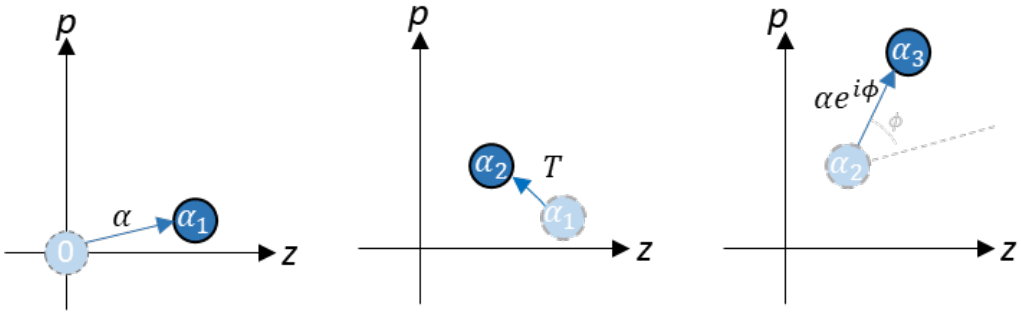

(a) Using delay time T

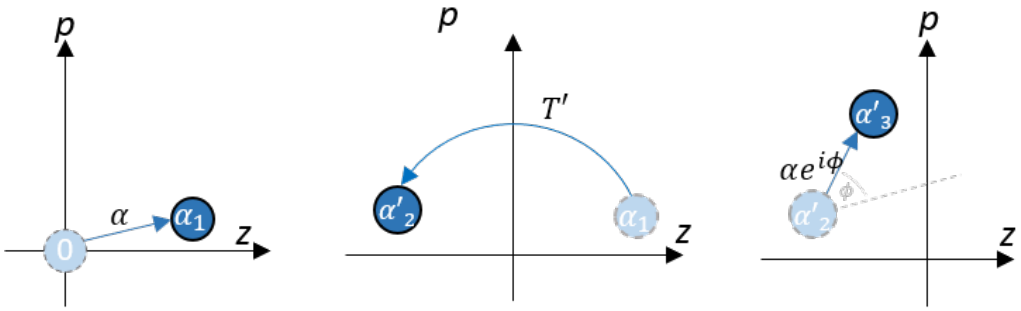

(b) Using delay time T'

Figure 4-5: Coherent State Free Precession Sequence, shown in the reference frame of the oscillator. Fig. 4-5(a) shows the sequence with a delay time T, while Fig. 4-5(b) uses a longer delay time of T' for comparison. From left to right: the ground harmonic oscillator state is displaced by α by a drive field with zero phase. The drive field is turned off, and the displaced state subject to decoherence moves in phase space during the delay time. Finally, the drive field, now with relative phase ϕ, again displaces the state by α. We measure the magnitude squared of the final state, $|\alpha_3|^2$ (or $|\alpha_3'|^2$ for Fig. 4-5(b)) to quantify the motional state. This magnitude corresponds to the radial distance from the origin to the coherent state in phase space.

The primary experimental advantage of this method is that it reduces optical addressing operations to the bare minimum of ground state initialization and state readout through sideband interactions and state-dependent fluorescence. Methods using sideband transitions to create superpositions of two Fock states or two coherent states are affected by internal state coherence times, such that the resulting measurement may not purely reflect the motional coherence of the system. Even Doppler-cooling-based displacements depend on the ion internal level structure to perform motional operations. In both cases, any laser operations are subject to potential errors such as misalignment of the laser to the trap, intensity gradients across the beam profile, and laser frequency errors and unlocking. This was particularly advantageous in our system, where an unexplained source of noise caused slow, random drifts of the ion and trap position relative to the laser beam. Although this will be discussed more in detail later, using the electrodes to drive the coherent states alleviated this concern.

Lastly, directly-driven coherent state sequences may show promise as an experimental benchmark in continuous-variable quantum computing (CVQC). Conventional quantum computing, as presented in this thesis, uses discrete quantum states, such as the ion's internal spin state or quantized motional state. However, an alternate field of CVQC exists, which uses quantum states described by continuous variables[LB99, WPGP$^+$12]. Examples include position, momentum, and the amplitude of an electric field. As in spin-1/2 Ramsey methods where the coherence times are influenced by laser stability, measurements from our motional sequences are influenced by the coherence of our electric drive field as well. Given that this drive field would serve to coherently control the ion motional modes and could therefore limit operation fidelity, our implementation of free evolution interferometry could serve as a method for quantifying the coherence of a CVQC system.

4.3.3 Free Precession Sequences under Unitary Evolution

To observe Ramsey-like oscillations by driving coherent states, we can use the phase-varying method described earlier. As displayed graphically in Figure 4-5, we can replace the $\pi/2$ pulses of a spin-1/2 Ramsey sequences with two coherent displace-

ments characterized by complex values α and $\alpha e^{i\phi}$ and separated by the delay time T. The two displacements are equal in magnitude, but differ by a relative phase ϕ, just like the spin-1/2 case. These displacements are generated by an electric drive field with Rabi strength Ω and a constant detuning δ applied for a time τ_d. Using the general formula for a coherent displacement $\alpha(t_0, \tau)$, given in Equation 4.9, for an initial time $t_0 = 0$, pulse time $\tau = \tau_d$, and initial state $\alpha(t_0) = 0$, we can define our coherent displacements as:

$$\alpha = i\Omega e^{i\phi} \frac{1 - e^{i\delta\tau_d}}{\delta} \tag{4.14}$$

On resonance, $\delta = 0$, and this equation simplifies to $\alpha = \Omega\tau_d e^{i\phi}$, and the final average motional quanta of the displaced state is [MKW+19]:

$$\begin{aligned} \bar{n} &= |\alpha|^2 \\ &= 2\left(\frac{\Omega}{\delta}\right)^2 [1 - \cos(\delta\tau_d)] \end{aligned} \tag{4.15}$$

We can phenomenologically model the results of this sequence on a coherent state amplitude for the cases of no damping, amplitude damping, and dephasing. By assuming a purely coherent state, the physics below are entirely classical dynamics even though a quantum analysis is employed. This simplified model does not require the use of density matrices, even though it considers decoherence effects.

Ideal Free Evolution

Consider the following sequence of transforms of the state of a simple Harmonic oscillator. Let the initial state be

$$|\psi_0\rangle = |0\rangle, \tag{4.16}$$

the ground state. We first displace the state (along a fixed axis, which defines our phase reference) by α, as defined in Equation 4.14 for $\phi = 0$, to produce

$$|\psi_1\rangle = |\alpha\rangle\,, \tag{4.17}$$

a coherent state with parameter α. This state is then allowed to evolve freely over time T, becoming

$$|\psi_2\rangle = |\alpha e^{i\delta T}\rangle\,, \tag{4.18}$$

We then displace the state again, along a direction determined by a phase ϕ, relative to the axis of the first displacement, again by amplitude α, obtaining

$$|\psi_3\rangle = |\alpha(e^{i\delta T} + e^{-i\phi})\rangle\,, \tag{4.19}$$

This is a coherent state with complex amplitude $\alpha_3 = \alpha(e^{i\delta T} + e^{-i\phi})$. If we then measure $\bar{n} = \langle\psi_3|\hat{N}|\psi_3\rangle$ as a function of ϕ, we obtain

$$\begin{aligned}
\langle\psi_3|\hat{N}|\psi_3\rangle &= |\alpha|^2\left(e^{-i\delta T} + e^{-i\phi}\right)\left(e^{i\delta T} + e^{i\phi}\right) && (4.20)\\
&= |\alpha|^2\left(2 + e^{i\phi - i\delta T} + e^{i\delta T - i\phi}\right) && (4.21)\\
&= |\alpha|^2\left(2 + 2\cos(\phi - \delta T)\right) && (4.22)\\
&= |2\alpha|^2\cos^2\left(\frac{\phi - \delta T}{2}\right)\,, && (4.23)
\end{aligned}$$

where the amplitude of the oscillations is $|2\alpha|^2$, and from our earlier definition for $|\alpha|^2$ in Equation 4.24, the amplitude becomes a function of the detuning:

$$\begin{aligned}
|2\alpha|^2 &= 4|\alpha|^2\\
&= 8\left(\frac{\Omega}{\delta}\right)^2\left[1 - \cos\left(\delta\tau_d\right)\right]
\end{aligned} \tag{4.24}$$

Thus, we achieve the maximum displacement of $\bar{n} = |2\alpha|^2 = |2\Omega\tau_d|^2$ on resonance with $\delta = 0$ when the drive phase difference is a multiple of 2π. For a nonzero detuning, the amplitude of the oscillations decreases and their maximum displacement occurs

when $\phi = \delta T$, as shown in Figure 4-6.

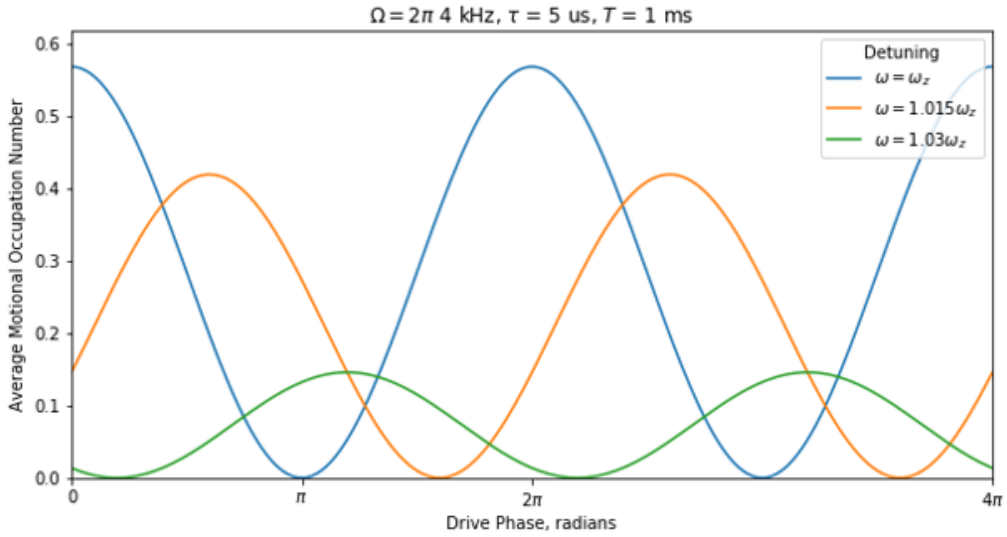

Figure 4-6: Simulation curves for the resultant motional state after a free precession sequence applied to an initial ground state for various drive frequency detunings. These curves can be generated using Equation 4.24.

Amplitude Damping

Now, what happens if $|\psi_2\rangle$ decays a bit during its free evolution time T? We might phenomenologically model this as an exponential decay of its coherent state amplitude, replacing the original $|\psi_2\rangle$ with

$$|\psi_2'\rangle = |\alpha e^{(-\Gamma + i\delta)T}\rangle\,, \tag{4.25}$$

where Γ is the damping rate. Continuing on with the same second displacement as above, and again assuming this displacement to be of the same magnitude as the first, as defined in Equation 4.24, we get for the final state

$$|\psi_3'\rangle = |\alpha e^{(-\Gamma + i\delta)T} + \alpha e^{i\phi}\rangle\,. \tag{4.26}$$

The final measurement then produces

$$\begin{aligned}
\langle\psi_3'|\hat{N}|\psi_3'\rangle &= |\alpha^2|\left(e^{(-\Gamma-i\delta)T}+e^{-i\phi}\right)\left(e^{(-\Gamma+i\delta)T}+e^{i\phi}\right) && (4.27)\\
&= |\alpha|^2\left(1+e^{-2\Gamma T}+e^{-\Gamma T-i(\delta T-\phi)}+e^{-\Gamma T+i(\delta T-\phi)}\right) && (4.28)\\
&= 2|\alpha|^2e^{-\Gamma T}\left[\cos(\phi-\delta T)+\cosh(\Gamma T)\right] && (4.29)\\
&= 2|\alpha|^2e^{-\Gamma T}\left[2(\cos(\phi-\delta T)+1)/2-1+\cosh(\Gamma T)\right] && (4.30)\\
&= 2|\alpha|^2e^{-\Gamma T}\left[2\cos^2\left(\frac{\phi-\delta T}{2}\right)-1+\cosh(\Gamma T)\right] && (4.31)\\
&= |2\alpha|^2\left[e^{-\Gamma T}\cos^2\left(\frac{\phi-\delta T}{2}\right)-\frac{e^{-\Gamma T}(1-\cosh\Gamma T)}{2}\right] && (4.32)\\
&= |2\alpha|^2\left[e^{-\Gamma T}\cos^2\left(\frac{\phi-\delta T}{2}\right)-\frac{e^{-\Gamma T}-(1+e^{-2\Gamma T})/2}{2}\right] && (4.33)\\
&= |2\alpha|^2\left[e^{-\Gamma T}\cos^2\left(\frac{\phi-\delta T}{2}\right)-\frac{2e^{-\Gamma T}-1-e^{-2\Gamma T}}{4}\right] && (4.34)\\
&= |2\alpha|^2\left[e^{-\Gamma T}\cos^2\left(\frac{\phi-\delta T}{2}\right)+\frac{1-2e^{-\Gamma T}+e^{-2\Gamma T}}{4}\right] && (4.35)
\end{aligned}$$

This is reasonable, in that when $\Gamma T=0$, the result reduces to the no-damping case above, and when $\Gamma T\to\infty$, the result is $|\alpha|^2$, which is the amplitude of the second displacement (the effect of the first having damped away, back to $|0\rangle$). During the delay period, the state decoheres relative to the drive field in all directions in phase space, with more decoherence occurring with longer delays. As a result, for very long delays, the decoherence relative to the drive frequency will result in the second drive pulse, on average, not coherently displacing the state and changing $\bar{n}$. Moreover, the damping reduces the amplitude of the oscillation of $\bar{n}$ with respect to ϕ, while also changing the midpoint of the oscillatory behavior. In particular, the midpoint is

$$\begin{aligned}
\langle\psi_3'|\hat{N}|\psi_3'\rangle_{1/2} &= |2\alpha^2|\left[\frac{e^{-\Gamma T}}{2}+\frac{1-2e^{-\Gamma T}+e^{-2\Gamma T}}{4}\right] && (4.36)\\
&= |2\alpha^2|\left[\frac{1+e^{-2\Gamma T}}{4}\right] && (4.37)\\
&= 2|\alpha^2|\left[\frac{1+e^{-2\Gamma T}}{2}\right] && (4.38)\\
&= 2|\alpha^2|\left(1-\Gamma T\right)+O(\Gamma^2) && (4.39)
\end{aligned}$$

where in the last line, we have expanded the expression to leading order in Γ. This shows that the midpoint starts drifting down. As Γ gets larger, this midpoint must drift all the way down to the asymptotic value of $|\alpha|^2$.

Dephasing

Another possible decoherence process is dephasing. Instead of a process affecting the magnitude of the coherent state amplitude, consider one that results in a loss of phase coherence between the coherent state and the drive field. Suppose that during the free evolution period, the oscillator is subject to a random phase kick; how does this affect the final measurement outcome? We may model this by applying a random phase rotation by angle θ, to $|\psi_2\rangle$, obtaining

$$|\tilde{\psi}_2\rangle = |\alpha e^{i\delta T + i\theta}\rangle\,, \tag{4.40}$$

where θ is drawn from a normal distribution with zero mean and standard deviation λ. The measurement result is then, averaging over this probability distribution:

$$\begin{aligned}\langle\tilde{\psi}_3|\hat{N}|\tilde{\psi}_3\rangle &= \frac{1}{\lambda\sqrt{2\pi}}\int_{-\infty}^{\infty}|2\alpha|^2\cos^2\left(\frac{\phi-\delta T-\theta}{2}\right)e^{-\theta^2/2\lambda^2}\,d\theta &(4.41)\\ &= |2\alpha|^2\left[\frac{1+e^{-\lambda^2/2}\cos(\phi-\delta T)}{2}\right], &(4.42)\end{aligned}$$

and this again is as expected: when $\lambda = 0$, this reduces to the no-dephasing outcome, and when $\lambda \to \infty$ this becomes $2|\alpha|^2$, because the phase is completely scrambled during the free evolution time. Note that this is different from the asymptotic outcome obtained for damping; moreover, the midpoint remains unchanged at $2|\alpha|^2$.

4.3.4 Free Precession Sequence with Open-System Dynamics

Although we have just phenomenologically derived the result for oscillations of coherent state magnitudes following our free precession sequence, creating a model for more general harmonic oscillator states and decoherence mechanisms will require open

system dynamics. This will involve solving the master equation for the time evolution of a density matrix with Linblad decoherence operators. A particularly relevant decoherence process is trapped ion heating, as presented in Section 4.2.2. We can refer back to the master equation in Linblad form, as shown in Equation 4.13, where this amplitude damping process is parametrized by the the heating rate Γ. We will consider this heating rate to be equivalent to the Γ used to represent amplitude damping in our analytical coherent state model, Equation 4.27, so that we can compare the results of the free precession oscillations for these two models. Solving the master equation for a general $\rho(t)$ analytically is difficult, but can be implemented in Python using the open source QuTip 4.5 software. This package contains a method *mesolve()* that solves for $\rho(t)$ given a Hamiltonian and a set of Linblad operators. Using the Hamiltonian in Equation (4.6) with $\hat{L}_e = \sqrt{2\Gamma(N+1)}\hat{a}$ and $\hat{L}_a = \sqrt{2\Gamma N}\hat{a}^\dagger$, we can sequentially solve for the state after each displacement and evolution period.

Despite the absence of an analytical model, our numerical QuTiP solutions show that in the presence of decoherence, the final $\bar{n}$ of a motional state after a free precession sequence with varying phase follows the expected sinusoidal behavior, with the normalized oscillation contrast decaying exponentially as $e^{(-\gamma T)}$, where γ is a generalized decoherence rate. These results, visualized in Figure 4-7, are analogous to those of the well-studied spin-1/2 Ramsey decay. By considering only the heating Linblad heating operators above with heating rate Γ, we find the decay going as $\gamma = \Gamma$. Additional decoherence operators will change this value of γ. This exponential decay result is supported by the general result for the time evolution of the heating function in Equation (4.13) from [IMPM03]. This paper found that the time evolution of the average thermal occupation of a harmonic oscillator subject to heating rate Γ goes as $\bar{n} = N(1 - e^{-\Gamma T})$, where N was the thermal average occupation number of the reservoir. The amplitude of the oscillations should be normalized relative to the amplitude of the zero-delay oscillations, since the amplitude of the $\bar{n}$ oscillations depend on the choice of α. Not normalizing these amplitudes would require an additional scaling factor in the decay fit that would make comparisons between experiments difficult.

Our simulations show that the normalized oscillation contrast decays with the

same rate Γ for both the numerical solution and the analytical model presented in Equation 4.27. The free precession oscillations look similar, but not exactly identical, due to the inclusion of the thermal reservoir with mean excitation number N in the numerical model. The analytical model oscillations correspond to the case of $N = 0$. In the numerical results, we find that the $\bar{n}$ oscillation curve, for a given delay time T, is uniformly shifted up by an additional term $N(1 - e^{-\Gamma T})$, which, not coincidentally, is the solution presented in [IMPM03] for the time evolution of a harmonic oscillator mean occupation number. In Figure 4-7, we use $N = 0$ for all delay times. An important note here is that the normalized contrast decay is unaffected by the value of N. The rate of decay is dictated by Γ, while N affects the final state which the harmonic oscillator tends towards. Lastly, our numerical simulations show that during

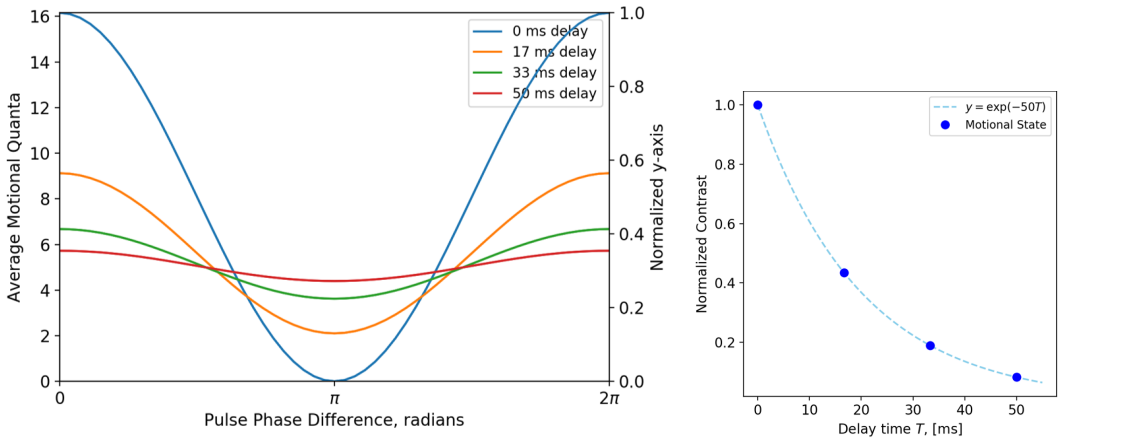

(a) Free Precession Oscillations

(b) Oscillation Contrast Decay

Figure 4-7: Simulated Oscillation Decay using $\Gamma = 50$, $\alpha = 2.01$, and $N = 0$. (a) Oscillations for various delay times, (b) Normalized oscillation contrast decay for the curves shown in (a). Normalization of contrasts is relative to the contrast of the zero delay point.

long delay times, the coherent state evolves to a thermal equilibrium state with the environment, characterized by the mean thermal excitation number N. After the second displacement, the distribution of number states within the final state will lie somewhere between a coherent and a displaced thermal state, the latter of which is defined in [SH96]. Our final state from the simulation is still characterized by an $\bar{n}$ that follows the oscillatory behavior described above. Although we lack an analytical

model to describe this final state, numerical simulation shows that the final number state distribution closely resembles that of a coherent state for shorter delay times, where the oscillation contrast is still visible within error for our experimental data shown later.

4.4 Internal State Readout

The average motional state $\bar{n}$ of a trapped-ion coherent state $|\alpha\rangle$ cannot be read out directly. We can only measure the internal state through repeated state-selective fluorescence detections. These repeated detections give us the probability that the ion is in the excited internal state. As a result, we need a mechanism to determine the coherent motional state from the ion's two-level internal state. Following the derivation used in [MKW$^+$19], a motional coherent state can be read out via a function that maps the average motional quanta $\bar{n}$ to the ion's internal excited state occupation probability. This is accomplished by considering the effect of applying an internal state red sideband laser pulse to a Poisson distribution of motional Fock states. After an arbitrary sequence of coherent displacements taking the initial state $|g,0\rangle$ to $|g,\bar{n}\rangle$, applying a RSB pulse of duration τ_{RSB} will excite the internal state to $|e\rangle$ with the following probability:

$$P_e(\bar{n}) = \frac{1}{2}\left[1 - P_0(\bar{n}) - \sum_{m=1}^{\infty} P_m(\bar{n}) \cos\left(2\Omega_{m,m-1}\tau_{RSB}\right)\right] \tag{4.43}$$

where $P_m(\bar{n})$ signifies the Poisson distribution over Fock states $|m\rangle$ with a $\bar{n}$ average. This is a simplification under the assumption that the state has been displaced to $|\bar{n}\rangle$ from the initial number state $|0\rangle$. A slightly more complicated form is required for cases where the initial number state is a higher motional state [MKW$^+$19], but the relevant displacements in this thesis are done from the initial ground state. $\Omega_{m,m-1}$ is the red sideband Rabi frequency corresponding to the $|g,m\rangle \leftrightarrow |e,m-1\rangle$. In contrast to a simplification of this value discussed earlier in this paper, a proper definition of the Rabi frequency includes also the Lamb-Dicke parameter η, the internal carrier

Rabi frequency Ω_0, and the generalized Laguerre polynomial $L^1_{m-1}(\eta^2)$:

$$\Omega_{m,m-1} = \Omega_0 e^{-\eta^2/2} \eta \sqrt{\frac{1}{m}} L^1_{m-1}\left(\eta^2\right) \tag{4.44}$$

As discussed in the previous section, the final number state distribution after our free precession sequences is not quite that of a coherent state, yet not that of a displaced thermal state either. However, for the delay times tested experimentally, we find it suitable to approximate the final state as a coherent state. Replacing the Poissonian number state distribution in Equation 4.43 with the numerically-generated final distribution from our simulation yielded nearly identical curves for P_e when fit to the experimental data. Due to this similarity, we may refer to the final state as a coherent state, although its Fock state distribution is not precisely described a Poissonian distribution.

This definition shows us that $P_e(\bar{n})$, as defined in Equation (4.43), is a non-monotonic function of $\bar{n}$ that also contains parameters η, Ω_0, and τ_{RSB}. These parameters all correspond to laboratory settings that can be chosen, calculated, or measured. We must first create the coherent state $|\alpha\rangle$ by turning on our electric drive field at ω for time τ_d with Rabi coupling strength Ω and phase ϕ. Note that Ω signifies the electric drive field Rabi coupling, while Ω_0 describes the internal carrier transition. We defined the magnitude of α earlier as a function of the fixed detuning $\delta = \omega - \omega_z$ in Equation 4.14. Assuming we are on resonance, $|\alpha| = \Omega\tau_d$. Although the exact value of Ω depends on multiple parameters, it is proportional to the electric drive field strength, so this means that we can either fix the drive strength or drive time, then scan the other variable to effectively scan $|\alpha|$ scaled by some numerical constant. Then by using $\bar{n} = |\alpha|^2$ in Equation (4.43), we are able to plot P_e as a function of α or τ_d, as in Figure 4-8, since $|\alpha|$ is proportional to τ_d when on resonance.

Converting from τ_d to α requires knowledge of the Rabi coupling strength Ω. This value can be determined by fitting $P_e(\tau_d)$ to experimental data, as done in Figure 4-8, it can also be determined by scanning the drive frequency ω over the resonant trap frequency ω_z. We can combine the functions $\alpha(\omega)$ and $P_e(\alpha)$ to get $P_e(\omega)$, and

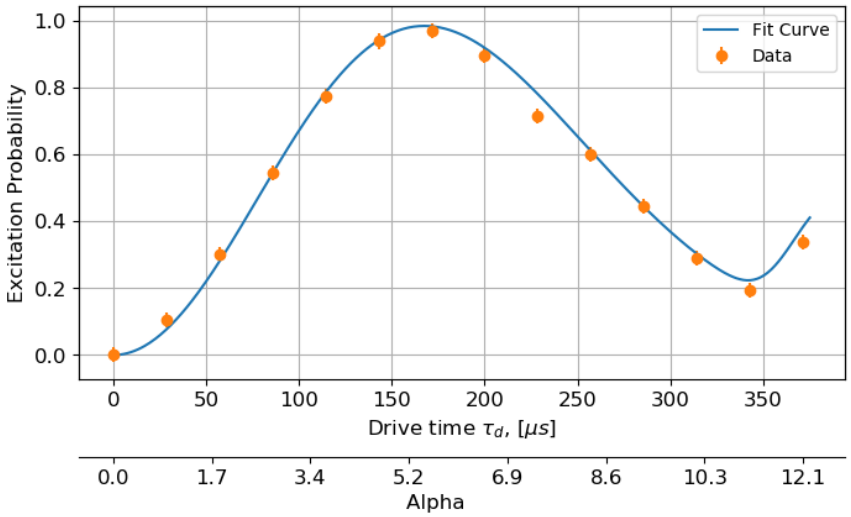

Figure 4-8: Internal state excitation probability as a function of coherent state magnitude $|\alpha|$ and drive time τ_d. The blue curve is a fit of Eq. (4.43) to experimental data points in orange. The resonant electric drive field with a fixed strength is turned on for a variable time τ_d, then the excitation probability is measured after applying a RSB pulse of time $\tau_{RSB} = 16$ μs. The fitted Rabi coupling frequency is $\Omega = 2\pi(5.17 \pm 0.03)$ kHz.

for a fixed known drive time and a fixed drive strength, we can then fit $P_e(\omega)$ to experimental data with Ω as the fit parameter, shown below in Figure 4-9. The Rabi coupling from our $P_e(\omega)$ fit matches the result from our earlier $P_e(\tau_d)$ to 0.1 kHz. As long as the maximum excitation probability on resonance, $P_e(\omega = \omega_z)$, remains in the first monotonic region of the experimentally-measured $P_e(\tau_d)$ curve shown earlier in Figure 4-8, our frequency scan $P_e(\omega)$ will show a characteristic $\text{sinc}^2(\omega)$ lineshape centered about ω_z, as shown below in Figure 4-9. The maximum excitation on resonance corresponds to a displaced state with $\bar{n} = |\alpha|^2 = (\Omega\tau_d)^2$.

Using the measurements and fits we have presented above, we can now perform our desired task of determining the motional state of the ion through measuring its internal state. We can simply take the fitted calibration curve for $P_e(\alpha)$ (shown earlier in Figure 4-8) to get a numerical monotonic function for $\alpha(P_e)$ and hence $\bar{n}(P_e)$. The only requirements from now on are that our electric drive field strength (proportional to Ω) and drive time remain such that our displacements of $|\alpha| = \Omega\tau_d$ remain in the first monotonic region of our experimentally measured $P_e(\alpha)$ curve

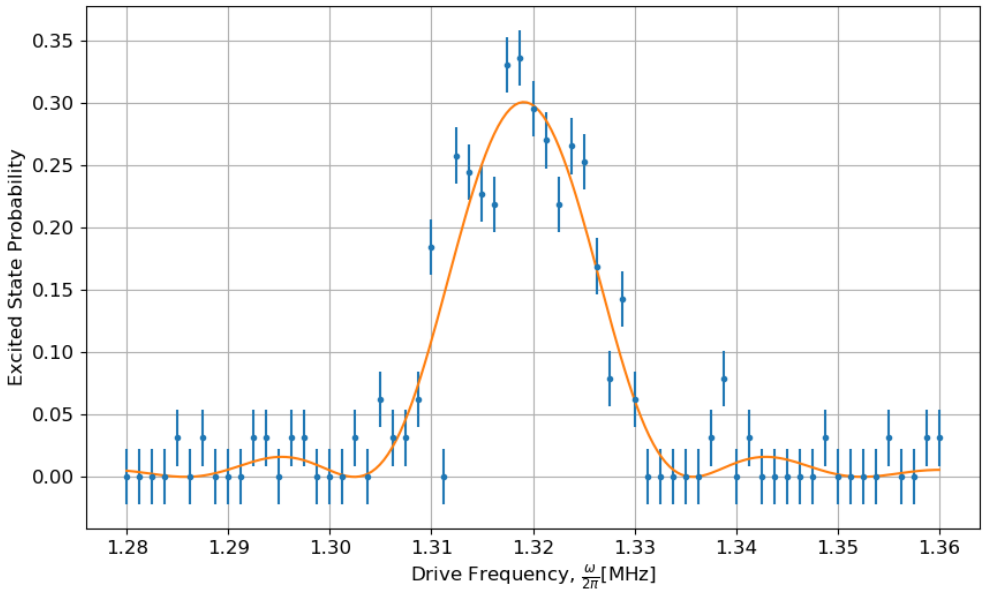

Figure 4-9: Experimental data points, in blue, for the internal state excitation probability P_e as a function of electric drive field frequency ω. A single displacement was applied for time $\tau_d = 60$ μs, then the excited state probability was read out after applying a single RSB pulse of time $\tau_{RSB} = 16$ μs. The orange curve is $P_e(\omega)$ is then fitted to the data points using the Rabi coupling Ω frequency as the fit parameter. The fit yielded $\Omega = 2\pi(5.1 \pm 0.1)$ kHz. The experimental error bars shown are $1-\sigma$ error bars for the measured data point.

and that the RSB drive time τ_{RSB} and internal state Rabi coupling Ω_0 both remain constant between the measurement of the $P_e(\alpha)$ calibration curve and the coherent drive experiment being performed. In the calibration curve, P_e is a non-monotonic

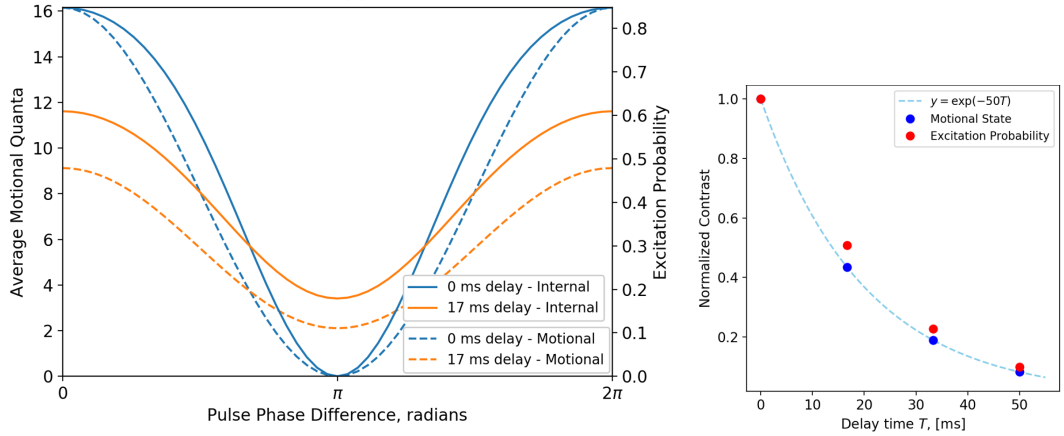

(a) Free Precession Oscillations (b) Oscillation Contrast Decay

Figure 4-10: Simulated Free Precession Oscillations using $\Gamma = 50$, $\alpha = 2.01$, $N = 0$. (a) Oscillations for 2 color-coded delay times, with the excitation probability shown on the solid curve and the previously-graphed motional state shown in dashed lines. (b) Comparing the normalized oscillation contrast decay for the excitation probability and the motional state.

and non-linear function of α. As a result, the measuring the excitation probability after a free precession sequence will not yield the characteristic $\cos^2(\phi_d/2)$ lineshape, as displayed free precession oscillation curves of Figure 4-7(a). Assuming that the magnitude of the displacement remains in the first monotonic region of the calibration curve, $P_e(\alpha)$ remains periodic over 2π, but there are nuances in the lineshape that can be determined by using one's calibration curve to convert from $\bar{n}$ to P_e, and backwards, as done in [TGD+16]. The differences between the curves are shown below in Figure 4-10(a), where the excitation probability is shown in the solid curves, in contrast to the $\cos^2(\phi/2)$ curve shown in the dashed lines, which were previously shown in Figure 4-7(a). The most notable consequence of this difference in lineshape is that the decay of the normalized P_e oscillation contrast does not follow an exponential decay for our calibration curve, shown in Figure 4-10(b). As a result, we must convert our excitation probability measurements to $\bar{n}$ before calculating oscillation contrasts and doing any contrast decay analysis.

Chapter 5

Experimental Procedure and Results

In this chapter, we detail the experimental steps required to implement our motional state free precession sequences, and we conclude by presenting the results of those experiments. In Section 5.1, we describe how we control and deliver the RF electric drive field used for coherent displacements. In Section 5.2, we outline our procedure for calibrating the drive strength, time, and frequency to ensure that we were generating the desired displacements. In Section 5.3, we list the complete sequence of laser pulses and drive field displacements used to prepare the ion, perform the free precession sequence, and read out its state. Finally, in Section 5.4, we present our measured data for the free precession sequences using four different delay times. Using this measured data, we extract a normalized oscillation contrast and display an exponential contrast decay, as predicted by our theory and simulations in Chapter 4.

5.1 Electric Drive Field Control

As previously presented in Section 3.3, our surface electrode trap allows us to deliver voltages to distinct groups of electrodes to generate particular electric field configurations at the location of the ion. To generate an RF drive field for our coherent displacements, we combined RF drive voltages with the existing DC trapping voltages for selected electrode groups via bias tees outside of the UHV chamber. To deliver the RF drive voltages, we selected two DC electrode groups, depicted in Figure 5-1, that

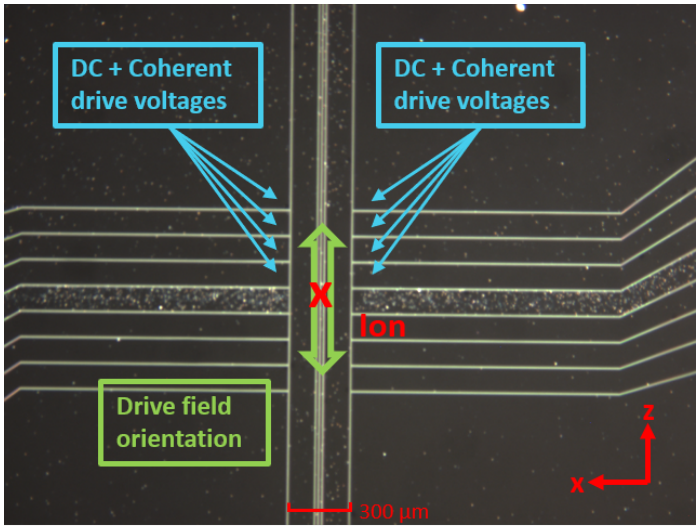

Figure 5-1: Microscope image of trap indicating the DC electrode groups that received the coherent drive RF voltages.

were geometrically symmetric across the trap axis (z-axis) such that their x-axis components perpendicular to the trapping axis would cancel, creating only an oscillating drive field on the same axis as the harmonic trapping potential. This ensured that we were primarily exciting the axial trapping modes of the ion's three-dimensional motion. Although the drive field is non-zero in the radial direction perpendicular to the trap, the drive frequency is far detuned from resonance with any radial modes, making radial excitation unlikely. To ensure that adequate RF voltages would pass through the low-pass filters on the ion trap tower prior to reaching the electrodes, as well as benefit from the higher signal-to-noise ratio in a higher-power DDS output, we applied large voltages on the order of volts to 10s of volts, followed by -30 dB of attenuation, before the bias tees. We then adjusted the digitally-controlled RF voltage amplitude (in arbitrary units) and attenuation to find an appropriate power where the ion would display some response for a reasonable drive time, typically on the order of 10 μs. For our displacements of $|\alpha|$ on the order of 1 with our Rabi frequency of approximately 5 kHz, our calculated electric drive field at the ion location was on the order of 0.1 mV/cm.

We used the ARTIQ (Advanced Real-Time Infrastructure for Quantum physics) system, developed my M-Labs, to control the delivery of RF voltages to the trap,

switch laser beams, and shift laser frequencies via AOM control. Its built-in DDS outputs were suitable for delivering the appropriate RF voltages to our AOMs as well as for our RF drive voltages delivered directly to the trap electrodes. ARTIQ hardware is run using the Python coding language, enabling us to develop individual scripts capable of controlling both the electric drive field and laser beams required for coherent drive operations and measurement.

5.2 Electric Drive Field Calibration Procedure

Following our general spectroscopy procedure of finding the carrier, first-order sideband, and optical pumping transitions to kHz accuracy, we had to calibrate the strength of our motion drive amplitude and time to determine the Rabi coupling frequency of the field, as well as ensure that our maximum coherent drive would remain in the first monotonic region of $P_e(\alpha)$, given by Equation (4.43) and displayed graphically in Figure 4-8. As discussed in the previous chapter, we would first scan the frequency of the coherent drive and identify resonant frequency at the center of the $\text{sinc}^2(\omega)$ function with accuracy ranging from 1-10 kHz, depending on the number of samples taken. Fitting Equation (4.43) to these data points would also yield an approximation for the Rabi frequency to a similar accuracy as the center frequency.

Using the resonant frequency identified from the previous scan, we would then scan the coherent drive time and measure the excitation probability. On resonance, $|\alpha| = |\Omega\tau_d|$, so this scan served the dual purpose of finding Ω, and hence $\alpha(\tau_d)$, after fitting the data to Equation (4.43), while also showing the maximum drive we could apply before overdriving the state into the non-monotonic region of Equation (4.43). The calibration curve displayed previously as Figure 4-8 would serve as the curve used to convert between P_e and α for the P_e data that would later be taken for this thesis. The settings used for this calibration curve, as well as the actual thesis data, involved a RSB probe time of $\tau_{RSB} = 16$ μs, the shortest time for which we could maximally excite our RSB transition, and a fitted motion drive Rabi coupling frequency of $\Omega = 2\pi(5.17 \pm 0.03)$ kHz.

We chose to set our coherent drive time and amplitude such that a single displacement yielded $|\alpha| = 2.1 \pm 0.2$, corresponding to $\bar{n} = 4.4 \pm 0.4$. Consequently, the maximum displacement that would occur during a free precession sequence was $2|\alpha| = 4.2 \pm 0.4$ and $\bar{n} = 16.7 \pm 0.7$. This maximal excitation would occur during the zero or near-zero delay sequences where the pulse phase difference was 0 or an integer multiple of 2π. In this case, the sequence would effectively act as two consecutive coherent displacements of $|\alpha|$. This was a suitable choice of $|\alpha|$ given the calibration curve in Figure 4-8. The expected maximal excitation, including error, would remain sufficiently below the maximum allowable α of the first monotonic region, approximately 5.5.

We also implemented a drive frequency stabilization protocol to correct for slow drifts in axial trap frequency during motion drive sequences. Early attempts at free precession sequences with long delay times or high drive powers found that the oscillations would gradually increase and decrease in frequency, which should not occur for oscillations as function of phase. They should remain periodic over 2π. In general Ramsey spectroscopy, deviations from this ideal periodicity typically indicate a detuning between the drive frequency and resonant frequency. Further measurements confirmed that the resonant trap frequency would drift as we applied increasing drive power or after we turned off the drive and waited for times much longer than the drive time. To obtain useful oscillations, we implemented a frequency stabilization procedure. For a given drive time, strength, and delay time, our stabilization script would conduct multiple trial sequences at the phase value corresponding to the steepest slope of the oscillations. This is a common protocol in frequency stabilization, since this steepest-slope point is the most responsive to frequency fluctuations while also indicating the direction in which the frequency has shifted. Using the result of the prior trial sequence, the script would incrementally change the drive frequency until the next trial sequence generated the expected result. Using the new resonant frequency, the actual data point would be taken. As a result of this stabilization procedure, data collection was rather slow. Anomalous errors such as ion loss, unexplained ion drifts relative to the laser beams, or laser frequencies drifting and unlocking would force us

to abandon the stabilization data for a sequence, forcing us to retake all data for those delay settings. As a result, we were only able to test 4 delay times - 1, 10, 20, and 50 ms. However, we achieve low error bars on our data points due to the high number of trials. In our initial unstabilized measurements, we found that the oscillations for zero delay and 1 ms delay were indistinguishable. Due to experimental challenges and time restrictions, we were unable to record a stabilized zero-delay sequence, but we find that the stabilized 1 ms delay data can effectively serve as a zero-delay reference.

5.3 Pulse Sequence

The applied pulse sequence, both laser and electric drive field, can be conceptualized in a convenient format depicted in Figure 5-2. A single free precession sequence

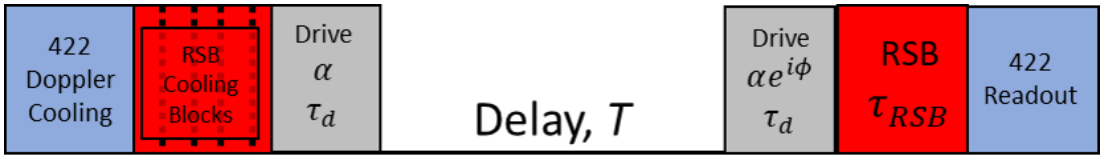

Figure 5-2: Diagram conceptually depicting the sequences of laser and drive field operations applied to the ion, reading from left to right in time. The blocks are not to scale in time.

begins with our usual state preparation for virtually any trapped ion operations: cooling and initialization to the motional and internal ground states $|g, 0\rangle$. An initial period of 422 nm Doppler cooling is applied to the ion, followed by a series of RSB pulses with durations gradually increasing from ~ 10 μs to ~ 20 μs, with each RSB pulse followed by a 1033 quench pulse lasting around 3 μs. Pulse durations would be slightly adjusted daily to account for changes in laser power or beam alignment. Due to the ion's thermal distribution of motional states, each with a different RSB Rabi frequency, multiple RSB durations must be used to cool all the motional states in the distribution to the ground state.

Following the initialization blocks, we begin our free precession sequence. We first apply our initial α displacement by turning on the RF drive voltage for time τ_d. We then turn off the RF voltage and wait for delay time T. We complete the sequence

by repeating our initial α displacement, but this time with a phase shift of ϕ_d relative to the first phase.

We conduct state readout using the RSB method describing in the previous chapter. Applying a single RSB pulse of duration τ_{RSB} to a distribution of motional states will put the internal state into a unique superposition of the ground and excited state. We read out this state as the excitation probability through state-dependent fluorescence detection with the 422 nm laser. Using our frequency stabilization script, many of these measurements are repeated for a single delay time and used for frequency adjustments. A smaller fraction are used for actual data collection. We then repeat the process for different phases and delay times to obtain a contrast decay curve.

5.4 Measured and Converted Results

The experimental results for our four frequency-stabilized sequences are displayed in Figure 5-3. Although the expected maximum excitations should occur for phases that are multiples of 2π, a uncontrolled phase-reset error in a new DDS caused a random phase offset for each sequence, in addition to the intended phase passed to the ARTIQ control. Since the phase offset was constant throughout a single free precession sequence, it only caused a horizontal shift in the data and did not affect the actual contrast or validity of the oscillations.

As explained at the conclusion of the previous chapter, the measured experimental $P_e(\phi_d)$ results of a sequence will not display the neat $\sin^2(\phi_d)$ behavior of $\bar{n}(\phi_d)$ sequences. Since we experimentally measure P_e, and not $\bar{n}$, our measured oscillation lineshape will depend on our calibration curve between α and P_e. The theoretical comparison between $\bar{n}(\phi_d)$ and $P_e(\phi_d)$ was previously displayed in Figure 4-10. We fit to the experimental $P_e(\phi_d)$ data shown above in Figure 5-3 by converting the expected $\bar{n}(\phi_d)$ curve into an excitation probability using our calibration curve. The data was then normalized relative to the maximum and minimum excitation of the 1-ms delay, where the results were effectively the same as a zero delay sequence. Details on this normalization, as well as the exact measured excitation probabilities and calculated

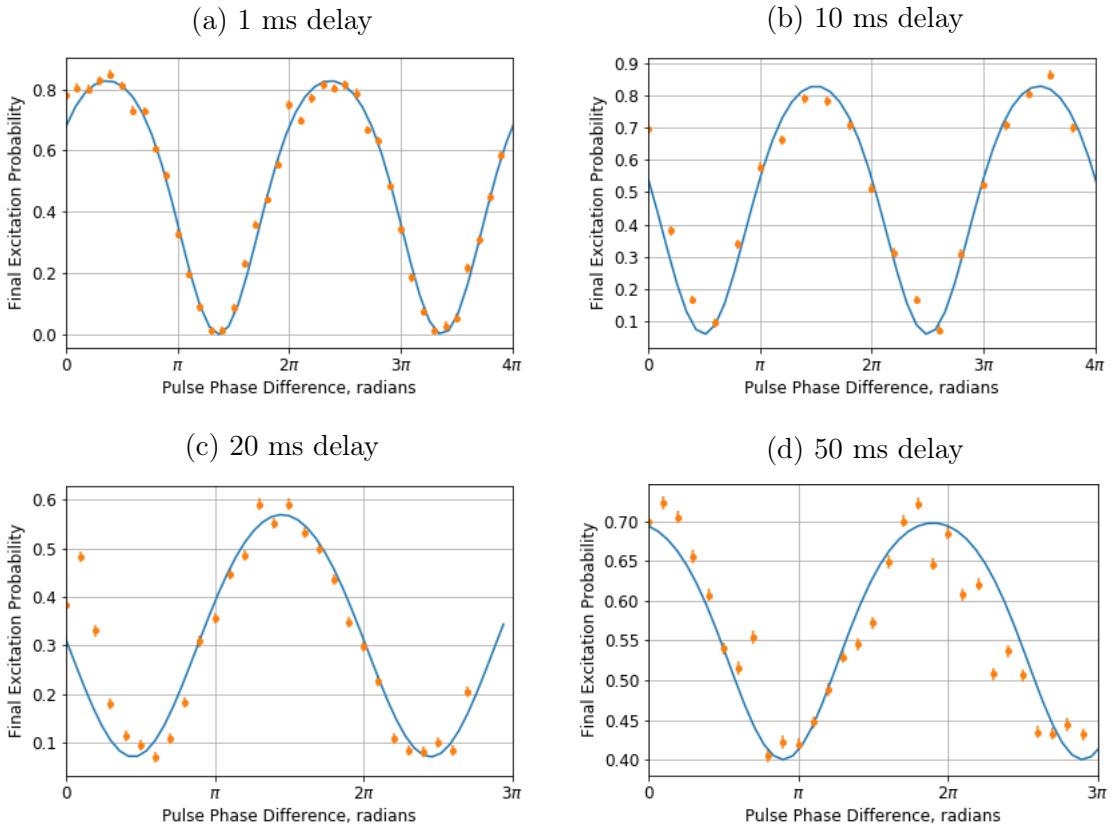

Figure 5-3: Experimental data points in orange for free precession sequences, with excitation probability as a function of drive phase difference, plotted for 4 different delay times. The fitted blue $P_e(\phi_d)$ curve is generated by converting the $\bar{n}(\phi_d)$ output from our QuTiP numerical simulation into P_e through our experimentally-generated $P_e(\alpha)$ calibration curve. The orange error bars represent a 1σ statistical uncertainty.

contrasts, are given in Appendix A.

By converting the measured probability contrasts in Figure 5-3 to normalized $\bar{n}$ contrasts, we can fit the oscillation contrast decay to an exponential of the form $\exp(-\gamma T)$ in Figure 5-4. Our fit finds that $\gamma = (24 \pm 5)\ s^{-1}$ for our experimental data.

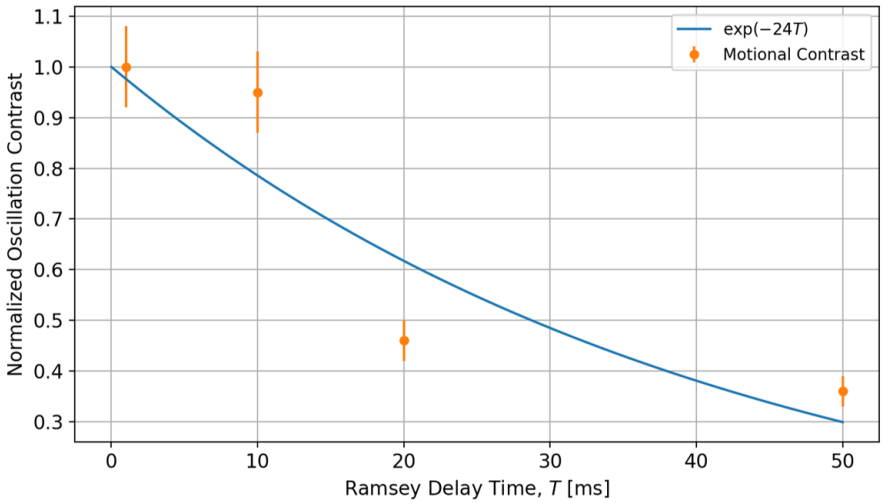

Figure 5-4: Free Precession Oscillation Contrast Decay with decay rate $\gamma = (24 \pm 5)\ s^{-1}$ for calculated normalized contrasts, obtained by converting the measured excitation probability data in Figure 5-3 to $\bar{n}$ using our $P_e(\bar{n})$ calibration curve. These conversions and data points are listed in Appendix A. The error bars reflect the uncertainty of the $P_e(\phi)$ fit curves for the raw data in Fig. 5-3, as well as the fit uncertainty in the calibration curve.

Chapter 6

Analysis and Conclusions

In this final chapter, we conclude by discussing the implications of our results for motional coherence measuremnt protocols, as well as look at improvements for future research. Section 6.1 analyzes measured result for the normalized oscillation contrast decay rate γ in terms of our open-system model for trapped ion heating, presented in Chapter 4. In Section 6.2, we identify specific experimental challenges that limited the accuracy of our data or hindered our data collection processes, then we suggest various improvements to address those issues in future tests. We also include possible variations on our free precession sequences, or different sequences altogether, that could help validate the results of this method and provide further insight to our procedure.

6.1 Analyzing the value of γ

A fitted decoherence rate of $\gamma = (24 \pm 5)\ s^{-1}$ suggests interesting conclusions about the dominant noise in our trapped ion system. As we displayed earlier in Figure 4-7, solving the master equation with heating Linblad operators parametrized by heating rate Γ will cause the free precession oscillation contrast to decay as $\exp(-\Gamma T)$. Using the sideband spectroscopy method to experimentally measure a heating rate in Figure 4-2, we previously determined our heating rate to be $\Gamma = (26 \pm 5)\ s^{-1}$.

The correspondence between γ and Γ implies that trapped ion heating may be the

dominant source of decoherence in our system. Solving the Linblad equation with our measured heating rate as the only source of decoherence would yield an exponential contrast decay almost identical to the fitted contrast decay from our experimental free precession sequence data. γ is a generalized decoherence rate describing different decoherence processes affecting the ion, not just heating. Assuming uncorrelated processes, we found through simulation that a pure dephasing rate of $\Gamma_{dephasing}$ in addition to a heating rate of Γ, would lead to a faster exponential contrast decay (larger γ) than the decay from the heating rate Γ alone. The fact that our fitted value for γ is nearly identical to our heating rate Γ, measured from sideband spectroscopy, suggests that these additional pure dephasing processes $\Gamma_{dephasing}$ are negligible compared to heating. The $\pm 5\ s^{-1}$ error on both γ and γ suggests the possibility of dephasing processes $\Gamma_{dephasing}$ existing on the order of $1\ s^{-1}$, but not show simply due to the magnitude of Γ. If the fitted decoherence rate γ was significantly longer than our measured heating rate Γ, we would need to include additional Linblad operators to account for some pure dephasing processes $\Gamma_{dephasing}$. However, our results are consistent with the conclusion that $\Gamma_{dephasing}$ is effectively zero, in comparison to the heating rate Γ.

6.2 Improvements and Further Experimentation

While our data leads to interesting conclusions regarding our system's motional coherence time, some experimental improvements could be made to yield additional results during future iterations of the motion drive protocol. One of the primary limiting factors of our current dataset was the small number of delay times tested. As discussed earlier, this was due to experimental setbacks that caused each set of data to take a long time while also requiring ideal laboratory conditions. The first of these include the problem of a changing trap frequency with long delays and large coherent drives. Although we circumvented this somewhat with a clever frequency stabilization scheme, more could be done in the future to understand the mechanism by which the coherent drive varies the static DC potentials to the point of significant

axial frequency shift. Perhaps this issue could be resolved through a different choice of DC trapping electrodes for delivery of the RF drive voltages to the ion. Such a change could alter the geometry of the electric drive field in a manner that may reduce our measured slow frequency drift.

Although specific to our trapped ion system, two additional setbacks included a short ion trapping lifetime and an unexplained slow drift in the trap position. These were particularly problematic because our frequency stabilization script could not handle these errors, causing us to abandon some data. The former issue is common amongst many ion trapping apparatuses, but can often be resolved. Stray field compensation, filtering of RF trapping voltages, ensuring proper UHV pressure are ways to eliminate fluctuations that can kick the ion from its harmonic potential. The slow ion drift, on the other hand, presents a unique challenge to our system. We have noticed an anomalous pattern of trap movement relative to the incoming external laser beams on our imaging camera. Given that the lasers beams are unlikely to drift in position, we postulate that some form of vibration is shifting the trap position at a slow, but non-negligible, rate. These non-linear drifts can cause the ion to move out its optimal addressing position for the 4 laser beams used during operations. Moving from this position causes a slew of problems, such as reduced Doppler cooling, lower ion fluorescence, and effective laser power fluctuations leading to fluctuations in the 674 nm beam Rabi coupling frequency. The reduced ion fluorescence was a major limitation on the efficacy of our frequency stabilization code. We have yet to determine the source of this trap drift, having already extensively searched for sources of vibration or motional coupling between the chamber and any mechanical connections it may have.

Other experimental factors of interest may reveal additional details about our free precession protocol or about one's trapped ion system. The parameters of the effective $\pi/2$ displacement of magnitude $|\alpha|$ is one such factor. On resonance, $|\alpha| = \Omega\tau_d$. In theory, one can arbitrarily choose any set of τ_d and Ω, determined through the amplitude of the RF drive voltage, yet still deliver the same coherent displacement, given that the parameters that satisfy the previous equation. In practice, this is

often not the case, as the signal-to-noise ratio may vary across RF voltage powers, or the precision of timing controls may be limited. We chose a set of τ_d and Ω that appeared reasonable for our system, but we did not quantify the effects of varying these two parameters in a controlled manner. It would be an interesting area of study to see how the coherent state production, manipulation, and measurement varies in a system for a fixed $|\alpha|$ but a variable τ_d and Ω. This would also be a useful experiment for determining whether the apparent trap frequency drift is exacerbated by longer drives, a more powerful drive field, or a combination of both factors. One could also consider the consequences of performing long drives that approach the timescale for decoherence, the inverse of the contrast decay rate.

To gain further understanding into the physical meaning of our fitted contrast decay, it would be worthwhile to later conduct a more conventional motional coherence measurement, namely a Ramsey sequence using a superposition of two motional states. As discussed earlier, this can be done with a superposition of Fock states or with cat states. These are well-studied methods for quantifying motional coherence, and comparing the measured Ramsey decay from these two-level methods versus our continuous coherent drive method may give us more insight on our results. Our coherent drive procedure could also be conducted on a system with a lower, or perhaps even a higher, heating rate than our sideband spectroscopy-measured rate of Γ. Using one with a lower heating rate may allow weaker dephasing processes $\Gamma_{dephasing}$ to become visible, while using one with a higher heating rate could verify that γ does in fact equal Γ for systems with ion heating as the dominant source of decoherence. For comparison, a similar free evolution sequence manipulating coherent states with Doppler cooling pulses was performed in [TGD$^+$16] with a trapped ion system with a notably higher heating rate than what we have observed in our system.

Lastly, this method shows promise for measuring coherence times using a continuous-variable quantum system, namely the amplitude of an electric field. This could enable CVQC to obtain coherence measurements in a method analogous to the use spin-1/2 Ramsey sequences to measure laser coherence.

Appendix A

Raw and Converted Measurement Data

The information below explains how we converted our experimentally-measured $P_e(\phi)$ free precession sequence data (displayed earlier in Figure 5-3 in Chapter 5) into normalized $\bar{n}$ oscillation contrasts, which were then used to demonstrate an exponential contrast decay (displayed earlier in Figure 5-4 in Chapter 5).

Table A.1: Table of Measured Excitation Probabilities

T [ms]	$P_{e,max}$	$P_{e,min}$
1	0.85 ± 0.05	0.02 ± 0.05
10	0.86 ± 0.07	0.12 ± 0.07
20	0.58 ± 0.05	0.10 ± 0.05
50	0.71 ± 0.04	0.41 ± 0.04

Using the $P_e(\phi)$ fit curves to our experimental data, we generated the maximum and minimum excitation probabilities $P_{e,min}$ and $P_{e,max}$ displayed in Table A.1. Then, using our $P_e(\alpha)$ calibration curve (displayed in Chapter 4 as Figure 4-8), we convert our measured $P_{e,min}$ and $P_{e,max}$ to $\bar{n}_{min}$ and $\bar{n}_{max}$ in Table A.2, where the fit error in the calibration curve is reflected in the error of these converted values.

Finally, normalization is achieved by taking all $\bar{n}$ values and scaling them relative to maximum and minimum $\bar{n}$ observed for the 1-ms delay, displayed mathematically in

Table A.2: Table of Converted & Normalized Motional Quanta

T [ms]	$\bar{n}_{max}$	$\bar{n}_{min}$	$\bar{n}_{max,norm}$	$\bar{n}_{min,norm}$	Normalized Contrast
1	16.7 ± 0.7	0.2 ± 1.0	1.00 ± 0.03	0.00 ± 0.05	1.00 ± 0.08
10	17.0 ± 0.9	1.4 ± 0.9	1.02 ± 0.04	0.07 ± 0.04	0.95 ± 0.08
20	8.7 ± 0.5	1.1 ± 0.6	0.52 ± 0.02	0.05 ± 0.02	0.46 ± 0.04
50	11.5 ± 0.4	5.5 ± 0.5	0.68 ± 0.01	0.32 ± 0.02	0.36 ± 0.03

Equation A.1 below. Ideally, this scaling should be done relative to zero-delay data points, but preliminary measurements found the the 1-ms and zero delay Ramsey sequence results to be identical. The normalized contrast, in the final column of Table A.2 is obtained by subtracting $\bar{n}_{max,norm}$ and $\bar{n}_{min,norm}$ for a given delay time T.

$$\bar{n}_{norm} = \frac{\bar{n} - 0.2}{16.7 - 0.2} \tag{A.1}$$

Appendix B

Release Statement

Massachusetts Institute of Technology Lincoln Laboratory Distribution Statement A: This work is approved for public release - distribution is unlimited.

Any opinions, interpretations, conclusions, and recommendations are those of the author, and do not reflect those of the United States government, the Department of Defense (DOD), or the Department of the Army. DOD approval for public thesis release does not imply DOD endorsement or factual accuracy of the presented material.

Bibliography

[AAB+19] F. Arute, K. Arya, R. Babbush, D. Bacon, J. Bardin, R. Barends, R. Biswas, S. Boixo, F. Brandao, D. Buell, B. Burkett, Y. Chen, Z. Chen, B. Chiaro, R. Collins, W. Courtney, A. Dunsworth, E. Farhi, B. Foxen, and J. Martinis. Quantum supremacy using a programmable superconducting processor. *Nature*, 574:505–510, Oct 2019.

[ABLW11] J. M. Amini, J. Britton, D. Liebfried, and D. J. Wineland. Microfabricated chip traps for ions. In *Atom Chips*, chapter 13, page 395–420. Wiley-VCH, Feb 2011.

[ASA+09] P. B. Antohi, D. Schuster, G. M. Akselrod, J. Labaziewicz, Y. Ge, Z. Lin, W. S. Bakr, and I. L. Chuang. Cryogenic ion trapping systems with surface-electrode traps. *Review of Scientific Instruments*, 80(1), Dec 2009.

[ATdS+16] M. M. Amaral, L. V. G. Tarelho, M. A. de Souza, A. C. Baratto, G. A. Garcia, S. T. Muller, J. De Martin, A. S. Rodriguez, A. Bebeachibuli, and D. V. Magalhães. Historical overview of ramsey spectroscopy and its relevance on time and frequency metrology. *Journal of Physics: Conference Series*, 733:012020, Jul 2016.

[BBC+95] A. Barenco, C. H. Bennett, R. Cleve, D. P. Divincenzo, N. Margolus, P. Shor, T. Sleator, J. A. Smolin, and H. Weinfurter. Elementary gates for quantum computation. *Physical Review A*, 52(5):3457–3467, Jan 1995.

[BCMS19] C. D. Bruzewicz, J. Chiaverini, R. Mcconnell, and J. M. Sage. Trapped-ion quantum computing: Progress and challenges. *Applied Physics Reviews*, 6(2), Apr 2019.

[BKM16] K. R Brown, J. Kim, and C. Monroe. Co-designing a scalable quantum computer with trapped atomic ions. *Nature Partner Journals - Quantum Information*, 2(1), Nov 2016.

[BKW18] I. A. Boldin, A. Kraft, and C. Wunderlich. Measuring anomalous heating in a planar ion trap with variable ion-surface separation. *Physical Review Letters*, 120:023201, Jan 2018.

[BMCS16] C. D. Bruzewicz, R. McConnell, J. Chiaverini, and J. M. Sage. Scalable loading of a two-dimensional trapped-ion array. *Nature Communications*, 7(1), Sep 2016.

[Bro07] M. Brownnutt. $^{88}Sr^{+}$ *Ion Trapping techniques and Technologies for Quantum Information Processing.* PhD thesis, Imperial College London Department of Physics, Sep 2007.

[BXN+17] A. Bermudez, X. Xu, R. Nigmatullin, J. O'Gorman, V. Negnevitsky, P. Schindler, T. Monz, U.G. Poschinger, C. Hempel, and J. Home. Assessing the progress of trapped-ion processors towards fault-tolerant quantum computation. *Physical Review X*, 7(4), Dec 2017.

[CBB+05] J. Chiaverini, R. B. Blakestad, J. Britton, J. D. Jost, C. Langer, D. Liebfried, R. Ozeri, and D. J. Wineland. Surface-electrode architecture for ion-trap quantum information processing. *Quantum Information and Computation*, 5(6):419–439, Sep 2005.

[Chw09] M. Chwalla. *Precision Spectroscopy with* $^{40}Ca^{+}$ *Ions in a Paul Trap.* PhD thesis, Innsbruck University Department of Experimental Physics, Apr 2009.

[CN65] P. Carruthers and M. M. Nieto. Coherent states and the forced quantum oscillator. *American Journal of Physics*, 33(7):537–544, Jan 1965.

[CS14] J. Chiaverini and J. M. Sage. Insensitivity of the rate of ion motional heating to trap-electrode material over a large temperature range. *Physical Review A*, 89:012318, Jan 2014.

[CZ95] J. I. Cirac and P. Zoller. Quantum computations with cold trapped ions. *Physical Review Letters*, 74:4091–4094, May 1995.

[DiV95] D. P. DiVincenzo. Two-bit gates are universal for quantum computation. *Physical Review A*, 51(2):1015–1022, Feb 1995.

[DiV00] D. P. DiVincenzo. The physical implementation of quantum computation. *Fortschritte der Physik*, 48(9-11):771–783, Mar 2000.

[dMFV96] R. L. de Matos Filho and W. Vogel. Even and odd coherent states of the motion of a trapped ion. *Physical Review Letters*, 76:608–611, Jan 1996.

[DMN13] S. J. Devitt, W. J. Munro, and K. Nemoto. Quantum error correction for beginners. *Reports on Progress in Physics*, 76(7):076001, Jun 2013.

[ESL+07] R. J. Epstein, S. Seidelin, D. Leibfried, J. H. Wesenberg, J. J. Bollinger, J. M. Amini, R. B. Blakestad, J. Britton, J. P. Home, W. M. Itano, J. D. Jost, E. Knill, C. Langer, R. Ozeri, N. Shiga, and D. J. Wineland. Simplified motional heating rate measurements of trapped ions. *Physical Review A*, 76:033411, Sep 2007.

[Fey82] R. P. Feynman. Simulating physics with computers. *International Journal of Theoretical Physics*, 21:467–488, Jun 1982.

[Gro96] L. K. Grover. A fast quantum mechanical algorithm for database search. In *Proceedings of the Twenty-Eighth Annual ACM Symposium on Theory of Computing*, STOC '96, page 212–219. Association for Computing Machinery, Jul 1996.

[HAB+14] T. P. Harty, D. T. C. Allcock, C. J. Ballance, L. Guidoni, H. A. Janacek, N. M. Linke, D. N. Stacey, and D. M. Lucas. High-fidelity preparation, gates, memory, and readout of a trapped-ion quantum bit. *Physical Review Letters*, 113(22), 2014.

[HCW+13] D. A. Hite, Y. Colombe, A. C. Wilson, D. T. C. Allcock, D. Leibfried, D. J. Wineland, and D. P. Pappas. Surface science for improved ion traps. *MRS Bulletin*, 38(10):826–833, 2013.

[HR87] S. Howard and S. K. Roy. Coherent states of a harmonic oscillator. *American Journal of Physics*, 55(12):1109–1117, Jan 1987.

[IMPM03] F. Intravaia, S. Maniscalco, J. Piilo, and A. Messina. Quantum theory of heating of a single trapped ion. *Physics Letters A*, 308:6–10, Feb 2003.

[JC12] L. Jiang and X. Chen. Quantum capacity region of simultaneous amplitude and phase damped qubit channel. *International Journal of Quantum Information*, 10(01):1250010, Feb 2012.

[KLS+20] V. Kaushal, B. Lekitsch, A. Stahl, J. Hilder, D. Pijn, C. Schmiegelow, A. Bermudez, M. Müller, F. Schmidt-Kaler, and U. Poschinger. Shuttling-based trapped-ion quantum information processing. *American Vacuum Society Quantum Science*, 2(1):014101, Mar 2020.

[KPM+05] J. Kim, S. Pau, Z. Ma, H. R. Mclellan, J. V. Gates, A. Kornblit, R. E. Slusher, R. M. Jopson, I. Kang, and M. Dinu. System design for large-scale ion trap quantum information processor. *Quantum Information and Computation*, 5(7):515–537, Nov 2005.

[Kri05] D. W. Kribs. A quantum computing primer for operator theorists. *Linear Algebra and its Applications*, 400:147–167, May 2005.

[LB99] S. Lloyd and S. L. Braunstein. Quantum computation over continuous variables. *Physical Review Letters*, 82, Feb 1999.

[LGRS04] V. Letchumanan, P. Gill, E. Riis, and A. G. Sinclair. Optical ramsey spectroscopy of a single trapped $^{88}Sr^{+}$ ion. *Physical Review A*, 70:033419, Sep 2004.

[LKH+07] D. M. Lucas, B. C. Keitch, J. P. Home, G. Imreh, M. J. McDonnell, D. N. Stacey, D. J. Szwer, and A. M. Steane. A long-lived memory qubit on a low-decoherence quantum bus. *arXiv e-prints*, page arXiv:0710.4421, Oct 2007.

[LMM+98] D. Leibfried, D. M. Meekhof, C. Monroe, B. E. King, W. M. Itano, and D. J. Wineland. Experimental preparation and measurement of quantum states of motion of a trapped atom. *Journal of Modern Optics*, 44(11-12):2485–2505, Jan 1998.

[MKW+19] K. C. McCormick, J. Keller, D. J. Wineland, A. C. Wilson, and D. Leibfried. Coherently displaced oscillator quantum states of a single trapped atom. *Quantum Science and Technology*, 4(2):024010, Mar 2019.

[MLM+19] P. Murali, N. M. Linke, M. Martonosi, A. Javadi Abhari, N. H. Nguyen, and C. Huerta Alderete. Full-Stack, Real-System Quantum Computer Studies: Architectural Comparisons and Design Insights. *arXiv e-prints*, page arXiv:1905.11349, May 2019.

[MSW+08] A. H. Myerson, D. J. Szwer, S. C. Webster, D. T. C. Allcock, M. J. Curtis, G. Imreh, J. A. Sherman, D. N. Stacey, A. M. Steane, and D. M. Lucas. High-fidelity readout of trapped-ion qubits. *Physical Review Letters*, 100(20), May 2008.

[MZMH19] K. K. Mehta, C. Zhang, S. Miller, and J. P. Home. Towards fast and scalable trapped-ion quantum logic with integrated photonics. In P. R. Hemmer, A. L. Migdall, and Z. U. Hasan, editors, *Advances in Photonics of Quantum Computing, Memory, and Communication XII*, volume 10933, pages 24–34. International Society for Optics and Photonics, SPIE, Mar 2019.

[Nie15] M. Niedermayr. *Cryogenic Surface Ion Traps*. PhD thesis, Innsbruck University Department of Experimental Physics, Jul 2015.

[NSSA+20] R. J. Niffenegger, J. Stuart, C. Sorace-Agaskar, D Kharas, S. Bramhavar, C. D. Bruzewicz, W. Loh, R. McConnell, D. Reens, G. N. West, J. M. Sage, and J. Chiaverini. Integrated optical control and enhanced coherence of ion qubits via multi-wavelength photonics. *arXiv e-prints*, page arXiv:2001.05052, Jan 2020.

[Pau90] W. Paul. Electromagnetic traps for charged and neutral particles. *Reviews of Modern Physics*, 62:531–540, Jul 1990.

[Pou11] G. Poulsen. *Sideband Cooling of Atomic and Molecular Ions*. PhD thesis, University of Aarhus Department of Physics and Astronomy, Nov 2011.

[RCM+08] C. Roos, M. Chwalla, T. Monz, P. Schindler, K. Kim, M. Riebe, and R. Blatt. *Laser Spectroscopy*, pages 53–62, Apr 2008.

[RPC+87] E. L. Raab, M. Prentiss, A. Cable, S. Chu, and D. E. Pritchard. Trapping of neutral sodium atoms with radiation pressure. *Physical Review Letters*, 59:2631–2634, Dec 1987.

[SH96] H. Saito and H. Hyuga. Relaxation of schrödinger cat states and displaced thermal states in a density operator representation. *Journal of the Physical Society of Japan*, 65(6):1648–1654, Jun 1996.

[Sho97] P. W. Shor. Polynomial-time algorithms for prime factorization and discrete logarithms on a quantum computer. *SIAM Journal on Computing*, 26(5):1484–1509, Oct 1997.

[SKC12] J. M. Sage, A. J. Kerman, and J. Chiaverini. Loading of a surface-electrode ion trap from a remote, precooled source. *Physical Review A*, 86:013417, Jul 2012.

[SSWH11] J. Siverns, L. Simkins, Seb Weidt, and W. Hensinger. On the application of radio frequency voltages to ion traps via helical resonators. *Applied Physics B*, 106, Jun 2011.

[Sta04] P. Staanum. *Quantum Optics with Trapped Calcium Ions*. PhD thesis, University of Aarhus Department of Physics and Astronomy, Feb 2004.

[SW95] T. Sleator and H. Weinfurter. Realizable universal quantum logic gates. *Physical Review Letters*, 74:4087–4090, May 1995.

[SW10] B. Schumacher and M. D. Westmoreland. *Quantum Processes, Systems, and Information*. Cambridge University Press, 2010.

[TGD+16] I. Talukdar, D. J. Gorman, N. Daniilidis, P. Schindler, S. Ebadi, H. Kaufmann, T. Zhang, and H. Häffner. Implications of surface noise for the motional coherence of trapped ions. *Physical Review A*, 93:043415, Apr 2016.

[TMK+00] Q. A. Turchette, C. J. Myatt, B. E. King, C. A. Sackett, D. Kielpinski, W. M. Itano, C. Monroe, and D. J. Wineland. Decoherence and decay of motional quantum states of a trapped atom coupled to engineered reservoirs. *Physical Review A*, 62(5), Oct 2000.

[TQ18] S. S. Tannu and M. K. Qureshi. A Case for Variability-Aware Policies for NISQ-Era Quantum Computers. *arXiv e-prints*, page arXiv:1805.10224, May 2018.

[VCLB06] K. Vant, J. Chiaverini, W. Lybarger, and D. J. Berkeland. Photoionization of strontium for trapped-ion quantum information processing. *arXiv e-prints*, pages arXiv:quant–ph/0607055, Jul 2006.

[WBD+19] K. Wright, K. Beck, S. Debnath, J. Amini, Y. Nam, N. Grzesiak, J. S. Chen, N. Pisenti, M. Chmielewski, C. Collins, K. Hudek, J. Mizrahi, J. Wong-Campos, S. Allen, J. Apisdorf, P. Solomon, M. Williams, A. Ducore, A. Blinov, and J. Kim. Benchmarking an 11-qubit quantum computer. *Nature Communications*, 10:5464, Nov 2019.

[WI79] D. J. Wineland and Wayne M. Itano. Laser cooling of atoms. *Physical Review A*, 20:1521–1540, Oct 1979.

[WMI+98] D. J. Wineland, C. Monroe, W. M. Itano, D. Leibfried, B. E. King, and D. M. Meekhof. Experimental issues in coherent quantum-state manipulation of trapped atomic ions. *Journal of Research of the National Institute of Standards and Technology*, 103:259–328, Jun 1998.

[WPGP+12] C. Weedbrook, S. Pirandola, R. García-Patrón, N. J. Cerf, Timothy C. Ralph, J. H. Shapiro, and S. Lloyd. Gaussian quantum information. *Reviews of Modern Physics*, 84:621–669, May 2012.

[WSH+19] F. Wolf, C. Shi, J. C. Heip, M. Gessner, L. Pezzè, A. Smerzi, M. Schulte, K. Hammerer, and P. O. Schmidt. Motional Fock states for quantum-enhanced amplitude and phase measurements with trapped ions. *Nature Communications*, 10(1), Feb 2019.

[Zhe98] S. Zheng. Preparation of motional macroscopic quantum-interference states of a trapped ion. *Physical Review A*, 58:761–763, Jul 1998.